Chemical Engineering Journal 537 (2026) 176188

Contents lists available at ScienceDirect

Chemical Engineering Journal

journal homepage: www.elsevier.com/locate/cej

Integrated computational fluid dynamics and experimental evaluation of a tubular membrane photoreactor for UVC-driven advanced oxidation at bench- and pilot-scale

Carla S. Santos [a], Paulo H. Marrocos [a], Claudio Passalía [b], Marisol D. Labas [b,c], Rodolfo J. Brandi [b,c], Rosa Montes [d], Rosario Rodil [d], José B. Quintana [d], Ana I. Gomes [a,*], Vítor J.P. Vilar [a,*]

[a] LSRE-LCM, ALiCE, Faculty of Engineering, University of Porto, Rua Dr. Roberto Frias, 4200-465, Porto, Portugal
[b] Departamento de Medio Ambiente, Facultad de Ingeniería y Ciencias Hídricas, Universidad Nacional del Litoral FICH/UNL, Santa Fe, Argentina
[c] Instituto de Desarrollo Tecnológico para la Industria Química - INTEC (CONICET/UNL), Güemes, 3450, Santa Fe, Argentina
[d] Aquatic One Health Research Center (ARCUS), Department of Analytical Chemistry, Nutrition and Food Sciences, R. Constantino Candeira S/N, IIAA building, Universidade de Santiago de Compostela, 15782, Santiago de Compostela, Spain

ARTICLE INFO

Keywords:
CFD simulation
Contaminants of emerging concern
Reflective surfaces
Residence time distribution
UV-driven advanced oxidation processes

ABSTRACT

This study combines computational fluid dynamics (CFD) simulations and experimental data to examine the hydrodynamic and photonic behavior of tubular membrane photoreactors operated under UVC and UVC/persulfate (UVC/PDS) conditions for the removal of organic micropollutants (OMPs). At bench-scale, CFD simulations revealed that the tangential inlet generated a helical flow pattern in the annular reaction zone (ARZ), promoting interaction between radial and axial velocity components. The effect of reflective surfaces on photon delivery was evaluated across three configurations: no reflector and one- and three-sided reflectors (N = 1 and N = 3). Reflective surfaces increased photon delivery to the ARZ, with the N = 3 configuration providing the highest optical efficiency and the best photolytic removal of the selected OMP in both demineralized water (DW) and conventional activated sludge (CAS) effluent. Based on these findings, a pilot-scale reactor preserving the same cross-sectional geometry and incorporating the N = 3 reflector was evaluated. Residence time distribution (RTD) experiments indicated a non-ideal plug flow with moderate axial dispersion, while CFD confirmed the persistence of the characteristic helical flow pattern. Under UVC alone, venlafaxine (VLX) removal remained limited, whereas under UVC/PDS operation removal exceeded 85% across all evaluated conditions. Simulations of the local volumetric rate of photon absorption (LVRPA) and spatial species distributions revealed a strong correlation between photon availability, oxidant distribution, and OMP degradation along the reactor length. These results provide valuable insights into the design of tubular membrane photoreactors and support their applicability for advanced urban wastewater treatment systems.

1. Introduction

In 2024, the European Union (EU) revised the Urban Wastewater Treatment Directive [1], encouraging the reuse of treated urban wastewater (UWW) while introducing more stringent requirements for the removal of organic micropollutants (OMPs) in large wastewater treatment plants (WWTPs). This updated regulatory framework highlights the urgent need to upgrade existing WWTP and adopt advanced treatment technologies capable of effectively addressing persistent OMPs [2,3]. UV-driven advanced oxidation processes (AOPs) have been widely demonstrated as effective polishing technologies for urban wastewater (UWW), capable of degrading OMPs that remain after conventional wastewater treatment processes [4–8]. Among the emerging treatment technologies, photo-activated sulfate radical-based advanced oxidation processes (SR-AOPs), including UVC/persulfate (UVC/PDS), have demonstrated strong potential as complementary solutions for advanced wastewater treatment [9–11]. However, despite their potential, the large implementation of photochemical processes in WWTPs remains limited due to high energy demands and operational efficiency

* Corresponding authors.
E-mail addresses: anaisa@fe.up.pt (A.I. Gomes), vilar@fe.up.pt (V.J.P. Vilar).

https://doi.org/10.1016/j.cej.2026.176188
Received 16 January 2026; Received in revised form 1 April 2026; Accepted 12 April 2026
Available online 13 April 2026

Nomenclature

A	Annular cross-sectional area, (m^2)
CAS	Conventional activated sludge effluent
c_0	Species concentration at the reactor inlet, (mol m^{-3})
$c(t)$	Species concentration as a function of time, (mol m^{-3})
D	Diameter, (m)
DW	Demineralized water
D_a	Axial dispersion coefficient, (m^2 s^{-1})
E	Residence time distribution, (s^{-1})
F	Cumulative residence time distribution
k_a	Absorption coefficient, (m^{-1})
L	Reactor length, (m)
LVRPA	Local volumetric photon absorption rate, (W m^{-3})
N	Number of sides in a flat reflector
P_i	Incident power, (W)
Pe	Péclet dimensionless number
Q	Flow rate, (m^3 s^{-1})
$q_{inc,i}$	incident radiation flux, (W m^{-2})
R	Net generation of species by chemical reaction, (kg m^{-3} s^{-1})
Re	Reynolds dimensionless number
t	Time, (s)
x, z	Cartesian coordinates, (m)
ε_{254nm}	Molar absorption coefficient at 254 nm, (M^{-1} m^{-1})
θ	Dimensionless time
χ	Dimensionless length
μ	Dynamic viscosity, (Pa·s)
σ_θ^2	Dimensionless variance
ρ	Fluid density, (kg m^{-3})
τ	Residence time, (s)
Φ	Dimensionless species concentration
Φ_{254nm}	Quantum yield at 254 nm, (mol Ein^{-1})

Subscripts

ARZ	Refers to the annular reaction zone
CS	Associated with cross-section
F	Refers to the feed stream
MS	Associated with the membrane surface
PDS	Related to sodium peroxydisulfate
QW	Associated with the quartz wall
R	Indicates a recirculation
Theoretical	Refers to a theoretical value
VLX	Related to venlafaxine

constraints [12].

Developing innovative photoreactors is thus crucial for achieving cost-effective photochemical treatment. However, the lack of high-performance, cost-effective photoreactor designs has been a major limiting factor in the industrial application of photochemical technology [13]. Reactor geometry strongly influences hydrodynamics, mass transfer, and photon utilization, which collectively determine system performance [12,14,15]. The bench-scale tubular membrane photoreactor proposed by Vilar et al. [16] has demonstrated high efficacy in removing OMPs from secondary-treated UWW within short residence times using various UV-driven AOPs [9,17–19]. The photoreactor design incorporates four low-pressure UVC lamps positioned equidistantly around a quartz tube, while a centrally located ceramic membrane, originally intended for filtration, serves as a longitudinal distributor, continuously supplying the oxidant (e.g., persulfate (PDS), hydrogen peroxide (H_2O_2), or ozone (O_3) through its porous structure. Because the membrane occupies the central region, external lamp arrangements are used instead of a central source as is typically found in tubular reactors. Considering this feature, a previous study by Martín-Sómer et al. [20] examined how different reflector geometries influence optical efficiency, defined as the fraction of emitted radiation reaching the reactor, in this photoreactor configuration. Various lamp/reactor arrangements were explored, including one-, two-, and three-sided flat reflectors (N = 1, N = 2, and N = 3, respectively), as well as circular and parabolic geometries. The results showed that optical efficiency was maximized when the distance between the lamp and the reactor was minimized. However, the extent to which these optical improvements enhance OMPs degradation has not yet been experimentally validated.

The photoreactor's hydrodynamic configuration further contributes to its performance. Tangential inlet and outlet pipes, oriented perpendicular to the flow direction, generate a helical liquid motion around the central membrane. This flow pattern promotes interaction between radial and axial velocity components, which may favor effective mixing and axial redistribution within the annular reaction zone (ARZ). To comprehensively characterize such systems, Computational Fluid Dynamics (CFD) emerges as a valuable tool for simulating both hydrodynamic and photonic phenomena and has been widely applied in the analysis and optimization of photoreactors and UV-based advanced oxidation systems [21–25]. A detailed hydrodynamic investigation of this reactor configuration was previously conducted by Caixeta et al. [26], combining experimental techniques with CFD simulations. Their results showed that the tangential inlet induces a helical flow structure associated with enhanced mixing and axial dispersion relative to purely axial flow. Similar trends have been reported for tubular reactors with tangential or swirling inlet configurations [27,28]. The residence time distribution (RTD) analysis confirmed that the reactor design promotes a predominantly mixed-flow regime governed by the interaction between radial and axial flows. However, the photonic performance of the reactor, specifically the spatial distribution and efficiency of incident radiation within the reaction domain, and its coupling with chemical reaction kinetics, remains unexplored.

This study combines CFD simulations with experimental validation to examine both the hydrodynamics and photon distribution in a bench-scale tubular membrane photoreactor. Among the reflector geometries proposed by Martín-Sómer et al. [20], selected configurations were experimentally tested using synthetic solutions and real activated sludge (CAS) effluent. Continuous-mode UVC photolysis tests were conducted to assess the removal of selected OMPs (including four target OMPs listed in Directive (EU) 2024/3019), to identify the most effective reflector configuration. These findings guided the construction of a pilot-scale unit developed as part of the EU-funded SERPIC project (Sustainable Electrochemical Reduction of Contaminants of Emerging Concern and Pathogens in Wastewater Treatment Plant Effluents for Crop Irrigation). This pilot unit was subsequently evaluated through CFD simulations and experimental testing, using venlafaxine (VLX) in synthetic water as a model OMP. At the pilot-scale, UVC photolysis and UVC/PDS treatments were applied in continuous mode to investigate degradation dynamics and reactive species interactions.

2. Materials and methods

2.1. Experimental setup

2.1.1. Tubular membrane photoreactor

The tubular membrane photoreactor comprises an internal ceramic ultrafiltration membrane (γ-Al_2O_3 membrane from Inopor® GmbH, Germany) with a molecular weight cut-off of 20 kDa, a pore size of 10 nm, and a porosity ranging 30% and 55%. In the bench-scale configuration, the membrane has an external diameter of 20 mm, an internal diameter of 16 mm, a total length of 200 mm, and an illuminated section

of 174 mm, corresponding to an illuminated treatment volume of 139.9 cm^3. Surrounding the membrane is an external quartz tube (supplied by E.VILA Projects & Supplies SL, Spain) with an outer diameter of 42 mm, an internal diameter of 38 mm, and total and illuminated lengths identical to those of the membrane (200 mm and 174 mm, respectively) (Fig. 1a). Compared to the bench-scale photoreactor, the pilot-scale photoreactor was constructed by increasing the length dimension, while maintaining all other geometrical properties unchanged. As a result, the quartz tube and ceramic membrane total length was 120 cm with an illuminated length of 117 cm, corresponding to an illuminated treatment volume of 946.9 cm^3 (Fig. 1b). In both systems, four low-pressure UVC mercury tubular lamps (λ = 254 nm) were symmetrically arranged around the quartz tube. In the bench-scale photoreactor, Puritec HNS 11 W G5 lamps (Osram) were used, with a nominal electrical power of 11.5 W and a UVC output of 2.6 W, as specified by the manufacturer. The pilot-scale photoreactor was equipped with TUV 75 W HO 1SL/6 lamps (Philips), presenting a nominal electrical power of 75 W and a UVC output of 25.5 W. However, for the pilot-scale experiments, the lamps were operated at a working power of 70 W. Assuming proportional emission characteristics, the estimated UVC output was calculated to be 23.8 W (theoretically, the 4 lamps emitted 95.6 W). The entire setup was enclosed within a capsule with different configurations lined with MIRO®4 UVC aluminum foil (spectral reflectivity approximately 90%, according to the manufacturer - Fig. SM-1) to enhance light reflection and prevent direct exposure to the radiation source.

2.1.2. Reflectors geometry

Based on the results of Mártin-Sómer et al. [20], the current study focused on the N = 1 and N = 3 geometries, both constructed from MIRO®4 UVC reflective aluminum sheets. Although the parabolic geometry offers higher optical efficiency, it was excluded due to manufacturing complexity, so only flat geometries were considered in this work. The N = 1 geometry was included as a simple and easily manufacturable design, serving as a baseline for comparison. The N = 3 geometry was selected as a balance between performance and feasibility, providing optical efficiency comparable to the parabolic reflector while being much easier and cost-effective to fabricate. To quantify the incident radiation reaching the ARZ of the photoreactor under each reflector configuration, actinometric tests were conducted using a circulating ferrioxalate solution in the ARZ, following the methodology described by Martín-Sómer et al. [20]. More details about the procedure applied can be found in the Supplementary material.

2.2. Experimental procedure

2.2.1. Bench-scale

The UVC photolysis experiments at a bench-scale were carried out in continuous mode with different matrices, namely: (i) demineralized water (DW) obtained from the Panice® system, and (ii) CAS effluent, collected at the outlet of the secondary settling tank of an urban WWTP located in northern Portugal. The essential physicochemical characteristics of CAS effluent and the analytical determinations/equipment employed are provided in Table SM-1 of the Supplementary material.

DW and CAS effluent were fortified with 10 μg L^{-1} of each of the 13 OMPs represented in Table 1. Stock solutions of each OMP were prepared in methanol or ultrapure water, according to the solubility of the compounds (OMPs were supplied by ACROS Organics, AlfaAesar, Sigma-Aldrich, and TCI (purity >95%)). The selected compounds were categorized as (very) persistent, (very) mobile, or (potentially) toxic, based on studies by Montes et al. [29] and Verlicchi et al. [30]. This group includes four compounds listed in the new UWWTD, namely Carbamazepine (an anticonvulsant), Diclofenac (an anti-inflammatory), Irbesartan (an angiotensin II receptor antagonist), and VLX (an antidepressant).

For DW experiments, three different reflector configurations were evaluated: (i) without a reflector, (ii) N = 1 geometry, and (iii) N = 3 geometry. The feed flow rate (Q_F) was set at 30 L h^{-1}, resulting in a residence time (τ) of 17 s. For experiments with CAS effluent, only N = 1 and N = 3 geometries are considered, and partial recirculation of the effluent was implemented to increase the liquid residence time within the photoreactor while maintaining the hydraulic conditions. Thus, for CAS experiments, both feed and recirculation flows were adjusted to maintain a consistent flow rate of 30 L h^{-1} in the ARZ, with Q_F set at 2.5 L h^{-1} and the recirculation flow rate (Q_R) at 27.5 L h^{-1}, resulting in a τ of 3 min 24 s. At this stage, no external oxidant was added to the system. All the conditions of the experiments performed in this work are summarized in Table 2.

When the four lamps were switched on, the effluent was continuously circulated from a cylindrical glass vessel to the ARZ using a gear pump (Ismatec BVP-Z). For the experiments with CAS effluent, another gear pump of the same model was coupled to the system to enable the partial recirculation of the effluent. For each experiment, samples were collected from the outlet of the photoreactor for OMPs analysis once steady-state conditions were reached (Fig. 1c). The OMPs were quantified through direct injection analysis by Acquity UPLC® liquid chromatograph interfaced to a XEVO TQD® triple quadrupole mass spectrometer equipped with an electrospray interface (ESI) from Waters (Milford, MA, USA). Further details can be found in Rodrigues-Silva et al. [18].

2.2.2. Pilot-scale

UVC photolysis and UVC/PDS tests were carried out in continuous mode, applying a Q_F of 30, 45, and 80 L h^{-1} (equivalent to a τ of 1 min 54 s, 1 min 18 s, and 42 s) under the conditions compiled in Table 2. In these tests, only the N = 3 geometry was considered. DW fortified with 20 mg L^{-1} of VLX ($C_{17}H_{27}NO_2$, TCI, >98%) was fed tangentially to the quartz tube wall and was continuously pumped via a gear pump (Ismatec BVP-Z) from a reservoir to the reactor (Fig. 1c). VLX was selected as the model pollutant due to its recent inclusion in the Directive (EU) 2024/319. Additionally, it frequently occurs at relevant concentrations in UWW in northern Portugal [31,32], reinforcing its environmental relevance and the need for effective removal strategies. The oxidant – commercial sodium peroxydisulfate ($Na_2S_2O_8$, Merck, ≥98%), PDS – was fed into the membrane via a LaPrep P130 pump, at a predefined flow rate to achieve a continuous dosing of 0.6 mM (Table 2), selected from previous studies using the tubular membrane photoreactor [17,19,33]. The tests began with the simultaneous activation of the effluent feed pump, the UVC lamps, and the oxidant dosing pump (for UVC/PDS tests). Once steady-state conditions were reached, samples were taken from the outlet of the tubular membrane photoreactor for VLX analysis (for more details, see Supplementary material). To prevent post-sampling oxidation, sodium sulfite (Na_2SO_3, VWR, 98%) was immediately added to the samples at a molar ratio of 5:1 in relation to the oxidant dose.

2.2.3. Residence time distribution (RTD)

Experiments were performed at pilot-scale for flow rates of 30 and 80 L h^{-1} (Reynolds numbers (Re) = 181 and 484, respectively). The Re was calculated as [26] (Eq. (1)),

$$Re = \frac{\rho}{\mu}\,\frac{Q_F}{A}\,(D_{QW} - D_{MS}) \quad (1)$$

where ρ is the water density (1000 kg m^{-3}), μ is the water molecular viscosity (1.0×10^{-3} Pa.s), Q_F is the feed flow rate (m^3 s^{-1}), A is the annular cross-sectional area (8.04×10^{-4} m^2), and D_{QW} and D_{MS} are the quartz wall inner diameter (0.0380 m) and the membrane outer diameter (0.0205 m), respectively.

A 0.0025% indigo carmine solution was used as a tracer. A positive step input method was applied to characterize the system response, followed by a negative step input to determine tracer elimination. The absorbance of the dye was measured at a wavelength of 588 nm using a

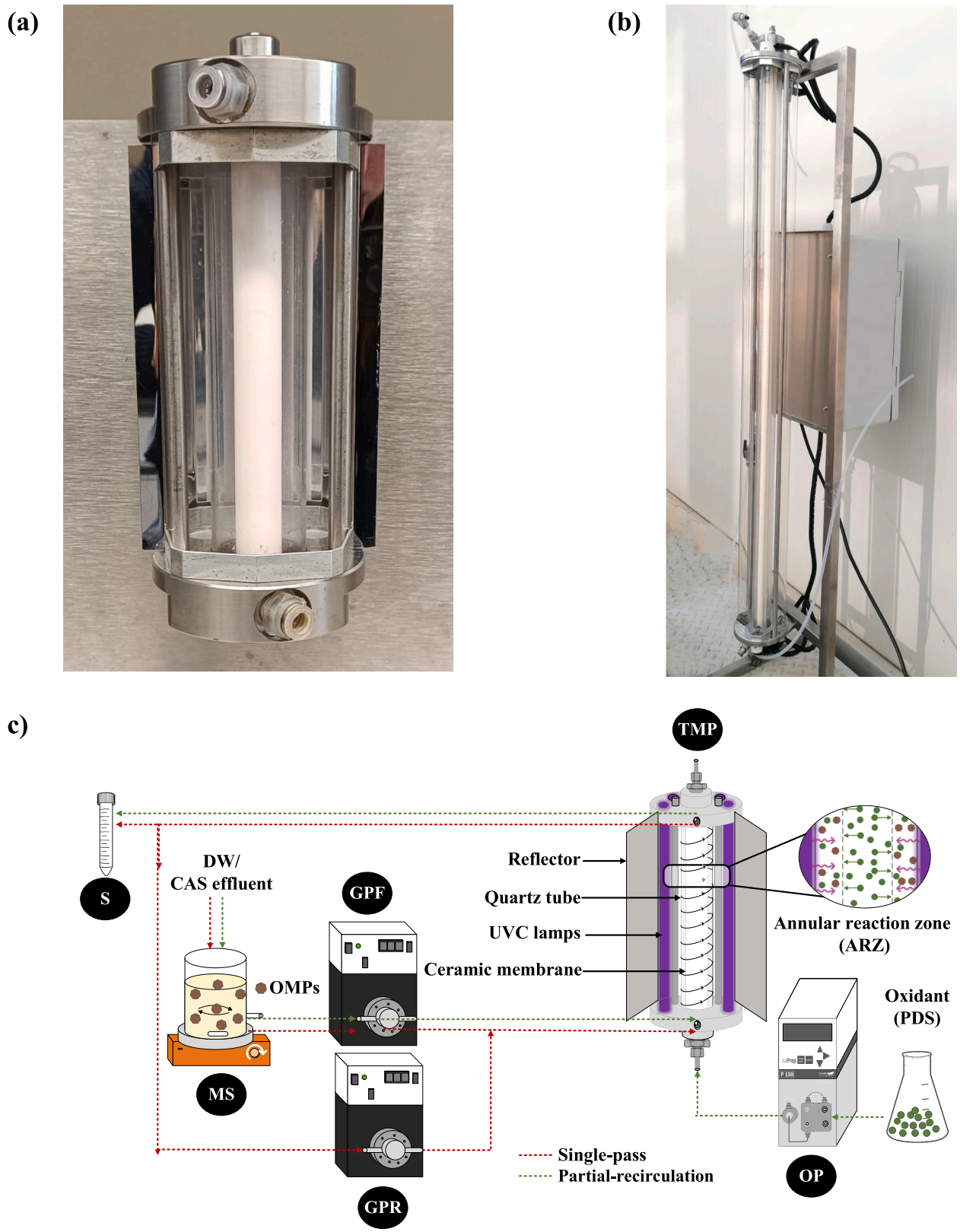

Fig. 1. Tubular membrane photoreactor photographs a) at bench-scale, b) pilot-scale, and c) simplified schematic of the tubular membrane photoreactor and experimental setup at single-pass (● ● ● ● ● ●) and partial-recirculation (● ● ● ● ● ●). Legend: GPF – Gear Pump - Feed; GPR – Gear Pump - Recirculation; MS – Magnetic Stirrer; OP – Oxidant Pump; S – Sampling; TMP – Tubular Membrane Photoreactor.

Table 1
Target OMPs selected for the bench-scale studies, respective molar extinction coefficient (ε_{254nm}) and quantum yield (Φ_{254nm}) at 254 nm, and limits of quantification (LOQ) in a DW and CAS effluent.

Category	Pollutant	Chemical composition	Molecular weight (g mol^{-1})	ε_{254} (M^{-1} cm^{-1})	Φ_{254} (mol Ein^{-1})	LOQ (μg L^{-1})	
						DW	CAS effluent
Angiotensin II receptor blockers	Valsartan	$C_{24}H_{29}N_5O_3$	435.52	2.1×10^3	Unknown	0.05	0.25
	Irbesartan	$C_{25}H_{28}N_6O$	428.53	1.5×10^4	Unknown	0.05	0.20
	Losartan	$C_{22}H_{22}ClKN_6O$	422.91	1.2×10^4	1.5×10^{-2}	0.15	0.80
Beta-blockers	Atenolol	$C_{14}H_{22}N_2O_3$	266.34	3.5×10^2	6.5×10^{-2}	0.10	0.15
	Bisoprolol	$C_{18}H_{31}NO_4$	325.44	Unknown	Unknown	0.01	0.15
Anticonvulsant	Carbamazepine	$C_{15}H_{12}N_2O$	236.27	5.8×10^3	3.3×10^{-3}	0.02	0.03
Flame retardants	Melamine	$C_3H_6N_6$	126.12	Unknown	Unknown	0.58	0.80
Herbicide	Diuron	$C_9H_{10}Cl_2N_2O$	233.10	1.6×10^4	1.4×10^{-2}	0.05	0.08
Insect repellent	DEET	$C_{12}H_{17}NO$	191.27	0.9×10^3	1.0×10^{-2}	0.03	0.03
Anti-inflammatory	Diclofenac	$C_{14}H_{10}Cl_2NNaO_2$	318.13	6.8×10^3	2.3×10^{-1}	0.02	0.25
X-ray contrast agent	Iopromide	$C_{18}H_{24}I_3N_3O_8$	791.11	2.2×10^4	3.9×10^{-2}	0.10	0.80
Antibiotic	Sulfamethoxazole	$C_{10}H_{11}N_3O_3S$	253.28	1.3×10^4	8.4×10^{-2}	0.01	0.10
Antidepressant	Venlafaxine	$C_{17}H_{27}NO_2$	277.40	3.8×10^2	9.7×10^{-2}	0.05	0.15

Table 2
Experimental conditions considered in bench- and pilot-scale testing.

Exp. (#)	Photoreactor	Matrix	Reflector geometry	UVC	PDS	$[PDS]_{ARZ}$ (mM)	Q_F (L h^{-1})	Q_R (L h^{-1})	Residence time
1	Bench-scale	DW	Without reflector	×	–	–	30	–	0 min 17 s
2			N = 1	×	–	–	30	–	
3			N = 3	×	–	–	30	–	
4		CAS effluent	N = 1	×	–	–	2.5	27.5	3 min 24 s
5			N = 3	×	–	–	2.5	27.5	
6	Pilot-scale	DW	N = 3	×	–	–	30	–	1 min 54 s
7				×	–	–	45	–	1 min 18 s
8				×	–	–	80	–	0 min 42 s
9				×	×	0.6	30	–	1 min 54 s
10				×	×	0.6	45	–	1 min 18 s
11				×	×	0.6	80	–	0 min 42 s

Legend: $[PDS]_{ARZ}$ – Persulfate concentration in the annular reaction zone; Q_F – Feed flow rate; Q_R – Recirculation flow rate.

Jenway 6300 spectrophotometer. An ISMATEC BVP-Z gear pump fed the inlet flow to the reactor. After passing through the reactor, the outflow was directed toward a continuous flow cell of the spectrophotometer via a Watson-Marlow 323 peristaltic pump before being discharged.

The experiment began by circulating water through the spectrophotometer cell. Data acquisition was initiated using LabVIEW™ software, and the corresponding absorbance was set as the baseline. Afterward, the dye was injected into the reactor. The time required for the tracer to flow through the system tubing was recorded and used to correct the RTD curves for this delay. The dye pump was switched off once the absorbance stabilized. Subsequently, the reactor was rinsed with water, and the corresponding time was recorded. The experiment was concluded when the absorbance dropped below 0.005.

The $F(t)$ curve was obtained by a normalization of the experimentally obtained outlet tracer concentration $c(t)$, as indicated in Eq. (2).

$$F(t) = \frac{c(t)}{\int_0^\infty c(t)dt} \tag{2}$$

Thereafter, the RTD was calculated according to Eq. (3), whereby a numerical derivation based on first-order finite differences was employed [34].

$$E(t) = \frac{c(t)}{\int_0^\infty c(t)dt} \tag{3}$$

Subsequently, to further characterize the mixing features of the flow, a one-dimensional Axial Dispersion Flow Model (ADFM) was applied. This model describes longitudinal mixing through a convection-diffusion transport, given by Eq. (4) [34].

$$\frac{\partial C}{\partial t} = -u\frac{\partial C}{\partial z} + D_a\frac{\partial^2 C}{\partial z^2} \tag{4}$$

The material balance comprises a transient term $\left(\frac{\partial C}{\partial t}\right)$, a convective transport term $\left(u\frac{\partial C}{\partial z}\right)$ and a diffusion transport term $\left(D_a\frac{\partial^2 C}{\partial z^2}\right)$, which accounts for the varying residence times of fluid elements along the axial direction through an axial dispersion coefficient, D_a [35]. The magnitude of the dispersion coefficients indicates the extent of deviation from ideal plug flow. By the introduction of dimensionless variables for time, spatial coordinate, and concentration ($\theta = t/\tau$, $\chi = \frac{z}{L}$, and $\Phi = \frac{c}{c_0}$, respectively), a dimensionless form of the differential equation is obtained, as represented in Eq. (5) [26],

$$\frac{\partial \Phi}{\partial \theta} = \frac{1}{\mathrm{Pe}}\frac{\partial^2 \Phi}{\partial \chi^2} - \frac{\partial \Phi}{\partial \chi} \tag{5}$$

where L and c_0 are the reactor length, and c_0, an initial concentration. The dimensionless Péclet number (Pe) compares the relative importance of convective and diffusive transport within the reactor and is defined as $\mathrm{Pe} = \frac{uL}{Da}$. Classical hydrodynamics indicates that $Pe \approx 1$ corresponds to mixed backflow, while $Pe > 50$ approaches plug flow [36]. Finally, the RTD of a tracer as a function of the θ and Pe is given by Eq. (6) [26].

$$E(\theta) = \Phi\,(\chi = 1, \theta) = \frac{1}{2}\sqrt{\frac{Pe}{\pi\theta^3}}\exp\left[\frac{-Pe\,(1-\theta^2)}{4\,\theta}\right] \tag{6}$$

2.3. Computational fluid dynamics simulations

CFD simulations were performed to obtain the hydrodynamic patterns and the spatial distribution of radiation in both bench- and pilot-scale reactors. This method enabled a detailed analysis of the flow pattern, mixing regimes, and photon distribution under different operational and geometric conditions. For the pilot-scale tubular membrane photoreactor, species transport and chemical reaction modeling were included.

2.3.1. Geometry, mesh, and models

Three-dimensional (3D) computational geometries of the tubular membrane photoreactor were developed for both reactors using ANSYS DesignModeler, accurately reproducing the conditions of the experimental setups. CFD simulations were conducted using ANSYS Fluent with a coupled multiphysics approach. For the bench-scale photoreactor, the objective of the simulation was to characterize the velocity field and the irradiance field. Fig. 2a shows the geometries and respective dimensions of the bench-scale photoreactor with N = 1 and N = 3 configurations. For the discretization of the computational domain, a 3D mesh was generated using ANSYS Meshing, with various local sizing functions applied to ensure adequate resolution in critical regions and a proper representation of the boundary layer. The mesh quality was evaluated using Skewness, Orthogonal Quality, Aspect Ratio, and Element Quality, yielding average values of Skewness = 0.3, Orthogonal Quality = 0.83, Aspect Ratio = 1.96, and Element Quality = 0.8, indicating good to excellent overall mesh quality.

A mesh convergence (grid independence) study was carried out to ensure the reliability of the numerical results. The analyses confirmed that the selected variables became independent of further mesh refinement, indicating that the solution was not affected by numerical discretization. The mesh generated with local mesh refinement has more than 3.8×10^5 elements. Additional details, including graphical results and a more comprehensive discussion of the convergence behavior, are provided in the Supplementary material (Fig. SM-2).

The flow was modeled using the laminar flow model. This methodological approach is particularly suitable for the operating conditions of the system, characterized by low Reynolds numbers where viscous forces predominate. The laminar flow model solves the Navier-Stokes equations directly, without the need for turbulence closure models, enabling the resolution of velocity and pressure fields within the reactor. However, curved and helical flow paths are an intrinsic characteristic of the flow in the photoreactor of this work, leading to enhanced radial mixing. Thus, an effective diffusion coefficient was introduced into the species transport equation to encapsulate the combined effects of molecular diffusion and radial mass transport within the reactor. All governing equations, source terms, and numerical implementations used in this work follow the formulations described in the ANSYS Fluent Theory Guide [37].

The radiation field was simulated using the Discrete Ordinates (DO) Radiation Model, which solves the Radiative Transfer Equation (RTE) to obtain the spatial and angular distribution of the radiation intensity within the computational domain [37]. The RTE was solved in 16 × 16 discrete angular directions, with a 4 × 4 pixels spatial discretization of the radiation control volumes, capturing the irradiance distribution within the fluid domain. Mesh convergence was also verified by testing different angular discretization's, yielding negligible differences in the predicted radiation field, as can be seen in the Supplementary material. Radiation absorption with solid boundaries (ceramic membrane and quartz tube) was not treated as a volumetric source term in the RTE but rather implemented through boundary conditions applied at the solid-fluid interfaces. This approach ensured that photon attenuation at material surfaces was correctly represented while preserving the physical meaning of the radiative transport equation in the fluid phase. The model thus resolved the spatial distribution of the radiation field within the reactor, enabling the evaluation of local photon availability.

For the tubular membrane photoreactor at pilot-scale, further considerations were made regarding the transport of PDS. The transport dynamics of the chemical species were described by a convection-diffusion equation, in which the effective diffusion coefficient

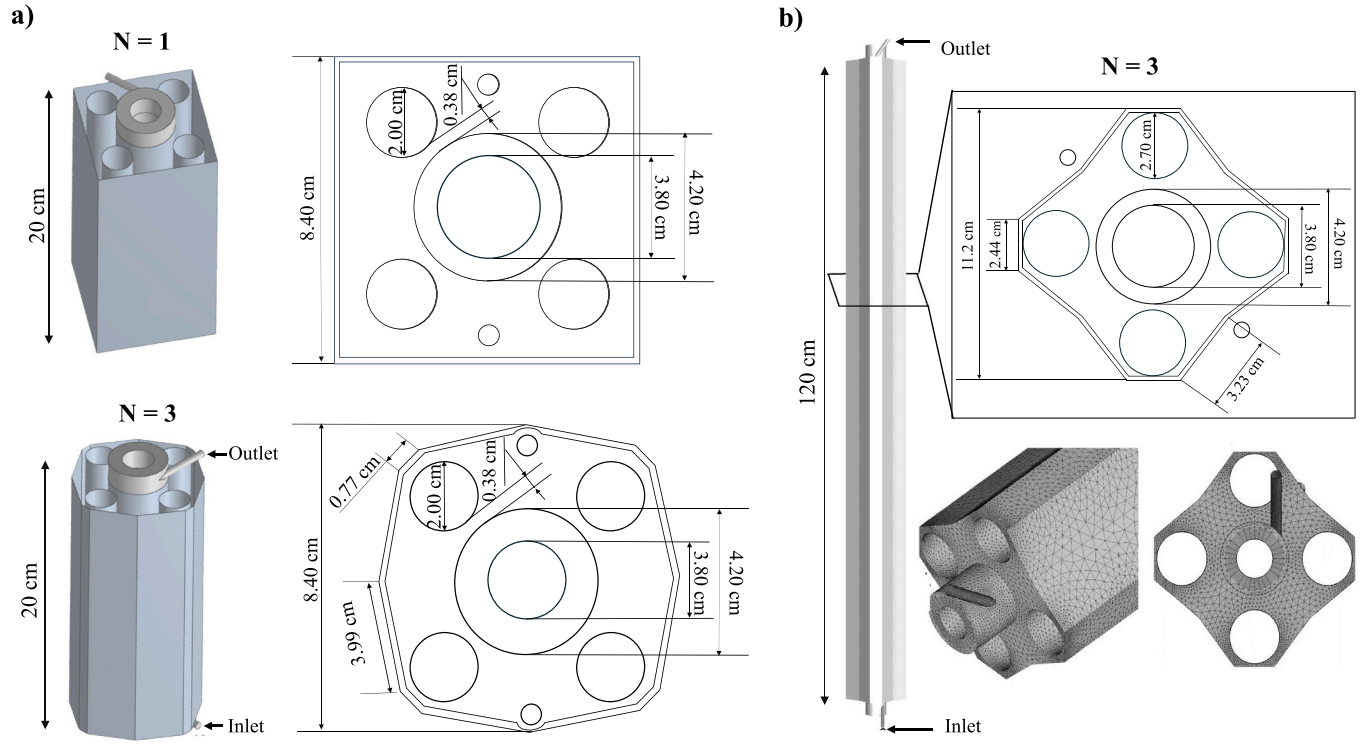

Fig. 2. Virtual geometries and respective dimensions of the tubular membrane photoreactor at (a) bench-scale and (b) pilot-scale, and mesh details for the N = 3 geometry.

accounted for the radial dispersion within the reactor domain. The concentration of PDS at the membrane wall was determined directly from experimental measurements, aligning with the value required to satisfactorily close the PDS mass balance under non-reactive conditions. This concentration was implemented as a boundary condition to ensure mass conservation within the model. The homogeneous chemical reactions were computed throughout the volume exposed to radiation, representing the interaction between a contaminant diluted in water and the oxidant continuously released from the inner wall, and activated by radiation. In this sense, the coupling of momentum transport, irradiance, and species concentrations accounted for the interactions between helical flow, radiation, and reaction kinetics, enabling a reliable prediction of concentration profiles and of the overall efficiency of the photochemical process.

The 3D geometry, its dimensions, and the mesh for N = 3 at pilot-scale are shown in Fig. 2b. In this case, the mesh incorporated various sizing controls and an inflation function, ensuring adequate resolution of the boundary layer and velocity gradients near the inner wall, as well as refinement in areas critical for chemical reactions. A mesh independence study, analogous to the bench-scale study, was conducted, confirming the reliability of the results as a function of mesh resolution. The mesh generated with local refinement consisted of approximately 9.5×10^5 elements. Mesh quality was also evaluated using metrics such as orthogonality, aspect ratio, skewness, and element quality, yielding average values very similar to those obtained in the bench-scale reactor. Further details on this analysis can be found in the Supplementary material (Fig. SM-2). The radiation field was obtained using the DO model with the same angular and spatial discretization as in the bench-scale device, ensuring consistency in irradiance prediction.

2.3.2. Boundary conditions

For simulations at both scales, a volumetric flow rate of 30 L h^{-1} was used in the ARZ, similar to the conditions applied in the experimental tests. In the bench-scale photoreactor, the fluid inlet was defined by a constant velocity boundary condition of 0.4 m s^{-1}, resulting in an inlet volumetric flow rate of 8.339×10^{-6} m^3 s^{-1} with the flow entering tangentially from the base of the reactor. For both scales, a zero-gauge pressure condition was applied at the outlets, and no-slip boundary conditions were used for all solid walls, with standard wall functions employed as the near-wall treatment. Specifically, for the pilot-scale photoreactor, an inlet velocity of 0.3 m s^{-1} was adopted. It is important to clarify that, although the volumetric flow rate remained constant, the velocity boundary condition differed because the inlet cross-sectional areas of the reactors were not identical. The fluid was initially considered at rest zero-gauge pressure and 20 °C throughout the domain, and isothermal conditions were assumed, as thermal effects were considered negligible in this study.

To solve the radiation field in the bench-scale photoreactor system, the liquid phase was treated as an absorbing, non-scattering medium, with a high absorption coefficient (k_a) of 3000 m^{-1}, a value compatible with an actinometer (the medium is modeled as a dilute aqueous solution). Between the lamps, reflector, and reactor, the medium is assumed to be air with its properties at ambient conditions (20 °C and 1 atm) including its refractive index of 1.00. Each UVC lamp was represented as a radiation source emitting at 254 nm, with radial emission consistent with the characteristics of low-pressure mercury lamps and an output power of 1.4 W (based on the ferrioxalate actinometries in Martín-Somer et al. [20]). Quartz was considered transparent to UVC at 254 nm, and, except for the reflective surface, all the other surfaces were defined with negligible reflectivity. Interactions involving radiation at solid-fluid interfaces were treated by applying radiative boundary conditions. In particular, the modeling of photon absorption and reflection at surfaces, including the membrane, quartz tube, and reactor walls, involved assigning appropriate optical properties (absorptivity and reflectivity) to each boundary. This approach accounts for photon attenuation at solid surfaces through surface interactions, rather than treating it as volumetric source terms within the radiation field equation, thus maintaining consistency with the principles of radiative transfer. The DO solution provided the local volumetric fluence rate, from which the local volumetric photon absorption rate (LVRPA) could be calculated in each control volume.

In the case of the pilot-scale photoreactor, the liquid was a mixture of two radiation-absorbing species diluted in water. Therefore, the refractive index of the mixture is assumed to be 1.33, and the molar absorption coefficient at 254 nm (ε_{254}) for each PDS and VLX was included ($\varepsilon_{254,PDS}$ = 21.1 M^{-1} cm^{-1} and $\varepsilon_{254,VLX}$ = 314 M^{-1} cm^{-1}, respectively). In this case, the lamps emitted 23.8 W each as a boundary condition. For the species balance, all ARZ walls were regarded as impermeable (no-flux), except in the UVC/PDS system, where the membrane surface was assumed to emit PDS uniformly and continuously. The PDS mass flow rate emitted was calculated under the assumption of no reaction in the liquid phase (ensuring mass consistency between the imposed PDS mass flux at the membrane surface and the resulting concentration within ARZ), corresponding to an outlet concentration of 0.6 mM ($[PDS]_{ARZ}$). A brief summary of all boundary conditions is presented in Table SM-2 of the Supplementary materials.

2.3.3. Photochemical kinetics and species transport

The photochemical degradation of PDS and VLX was described using a radiation-dependent kinetic model integrated within the CFD framework. Species transport was governed by the radiation-dependent kinetic model, with reaction terms implemented as source terms under the boundary conditions described in Section 2.3.2. As a reference case, simulations without reaction terms were first performed to confirm constant concentration profiles along the reactor, ensuring consistency of the transport formulation. The reaction kinetics were formulated as a function of the local volumetric rate of photon absorption (LVRPA), thereby directly coupling radiation transport with chemical reactions. The decomposition rates of PDS and VLX were expressed by the Eqs. (7) and (8), respectively.

$$r_{PDS} = -k_{PDS}\, LVRPA_{PDS} \tag{7}$$

$$r_{VLX} = -k_{VLX}\, LVRPA_{PDS}[VLX] - k_{Ph,VLX}\, LVRPA_{VLX} \tag{8}$$

where r_{PDS} and r_{VLX} denote the decomposition rates of PDS and VLX, respectively; k_{PDS}, k_{VLX} and $k_{Ph,VLX}$ are the kinetic constants for PDS degradation, VLX degradation via radical species, and VLX degradation by direct photolysis, respectively; $LVRPA_{PDS}$ and $LVRPA_{VLX}$ represent the local volumetric photon absorption rates by PDS and VLX, respectively; and $[VLX]$ represents the local concentration of VLX.

The LVRPA terms for each species were calculated for PDS and VLX, applying Eqs. (9) and (10), respectively.

$$LVRPA_{PDS} = \varepsilon_{PDS}\,[PDS]\,G \tag{9}$$

$$LVRPA_{VLX} = \varepsilon_{VLX}\,[VLX]\,G \tag{10}$$

where ε_{PDS} and ε_{VLX} are the molar absorption coefficients of PDS and VLX, respectively ($\varepsilon_{254,PDS}$ = 21.1 M^{-1} cm^{-1} and $\varepsilon_{254,VLX}$ = 314 M^{-1} cm^{-1}, respectively); and G is the incident radiation on the reaction zone. This formulation links the radiation field to the reaction kinetics through local photon absorption, accounting for spatial variations in irradiance and species concentration within the reactor. The kinetic parameters were determined by fitting the model to experimental data, and the resulting model reproduced the observed trends in PDS and VLX concentrations under different operating conditions.

2.3.4. Hardware capabilities and solution methods

All numerical simulations were conducted using the academic version of the ANSYS Fluent 19. Simulations were executed on a 6 Core Intel(R) Core(TM) i7-10750H CPU @ 2.80 GHz, running Windows 11 (64 bits) with 16 GB RAM. The device had a computational capacity of

669 Gflops. The simulations employed a steady-state, pressure-based solver, assuming an incompressible, Newtonian fluid and an isothermal condition at room temperature.

3. Results and discussion

3.1. Bench-scale tubular membrane photoreactor

3.1.1. CFD simulation: flow pattern

To study the flow pattern and elucidate the mixing mechanisms promoted by the tubular membrane photoreactor design, CFD simulations of the hydrodynamic field within the bench-scale system were conducted. Fig. 3a shows a map of the velocity vector field, illustrating the spatial distribution of fluid velocity within the reactor. The highest velocities occur at both inlet and outlet, located at the bottom and top of the photoreactor, respectively, where the flow is constrained to a narrow cross-sectional area. Along the vertical axis a gradual decrease in velocity is observed, with lower magnitudes in the upper sections of the reactor.

At the inlet, a uniform velocity profile was imposed as a boundary condition, corresponding to the prescribed flow rate. At the outlet, the contraction between the annular region and the outlet duct leads to the development of a non-uniform (parabolic-like) velocity profile, with higher velocities at the centerline and lower velocities near the walls due to the no-slip condition. Consequently, local velocities at the outlet can exceed those at the inlet, while the cross-sectional average velocity remains consistent with mass conservation.

The corresponding pathlines (Fig. 3b) confirm the establishment of a helical flow regime, induced by the tangential fluid inlet in combination with the reactor geometry. However, the rotational motion of the fluid is more intense near the inlet and gradually weakens toward the outlet. This attenuation correlates with the progressive reduction in the velocity magnitude along the axial direction, indicating that the initial rotational energy imparted by the tangential entry is gradually dissipated through friction at the reactor wall and the membrane surface, thus reducing the intensity of swirl as the fluid ascends. Nechita et al. [38] reported that such a spiral trajectory promotes a flow behavior tending toward a perfectly mixed regime, favoring broader dispersion of fluid elements and a wider range of residence times. Such hydrodynamic conditions can be particularly favorable for oxidation processes, as they improve the contact between the target micropollutants and reactive species, thereby enhancing the degradation efficiency of OMPs.

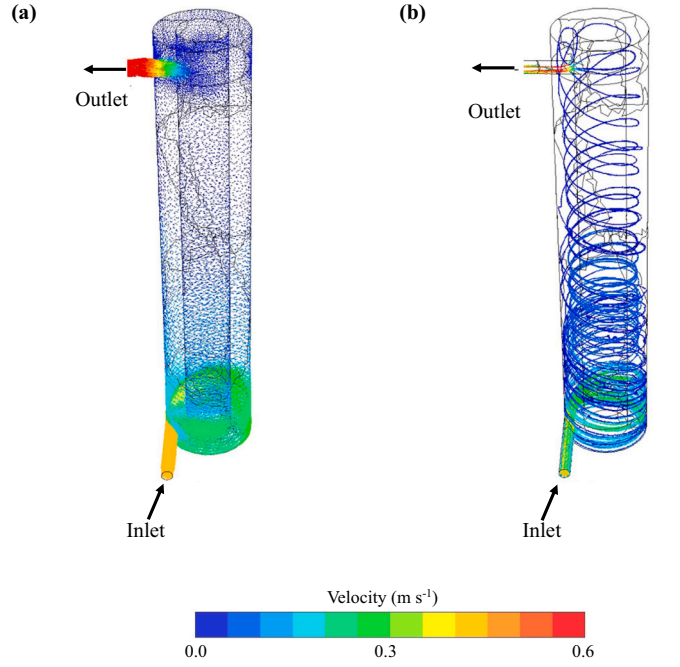

Fig. 3. Velocity field associated with a fluid flow in the bench-scale tubular membrane photoreactor at Q_F = 30 L h^{-1} represented by (a) velocity vector map and (b) pathlines trajectories.

3.1.2. CFD simulation: impact of reflector geometry in the photon field

Quantifying incident radiation power through actinometric tests is a crucial step for correctly interpreting photochemical process efficiencies [39]. In addition, CFD modeling of the photonic field enables visualization of the radiation field distribution within the reactor, providing a detailed understanding of the homogeneity of the illumination and the influence of reflector design. While actinometric measurements provide an estimate of the total radiation reaching the reactor, CFD simulations allow the spatial distribution of radiation intensity within the ARZ to be solved. The photonic balance analysis enabled the estimation of the fraction of radiation emitted by the lamps that effectively reached the reactor interior. The incident power (P_i) on each system surface was calculated using Eq. (11),

$$P_i = \int_{A_i}^{0} q_{inc,i}\, dA_i \tag{11}$$

where $q_{inc,i}$ represents the incident radiation flux and A_i is the area of the respective surface element. Based on ferrioxalate actinometric tests, each low-pressure UVC mercury lamp delivered a power output of 1.4 W [20], resulting in a total emitted power of 5.6 W for the four-lamp system. In the radiation model, the lamps were represented as linear sources with radial emission, consistent with the emission characteristics of low-pressure mercury lamps. A uniform emission along the lamp length was assumed for the source term, while the spatial distribution of radiation within the reactor was resolved using the DO model. Direct experimental validation of the internal spatial radiation distribution was not performed and remains a limitation of the present study.

From CFD simulations, Fig. 4a–c illustrates the incident radiation fields for three conditions: no-reflector, N = 1, and N = 3. It was established that the absence of a reflector severely constrains photonic utilization. Actinometric measurements demonstrated an incident power of 1.42 ± 0.01 W, corresponding to an optical efficiency of 25%. These findings align with those reported by Mártin-Sómer et al. [20], who observed an optical efficiency of 22% under similar no-reflector conditions. In contrast, for the reflector configurations with N = 1 and N = 3, the actinometric measurements revealed higher incident powers of 2.7 ± 0.1 W (N = 1) and 2.97 ± 0.01 W (N = 3), translating to optical efficiencies of 47% and 52%, respectively. These results are consistent with the optical efficiencies of 46% and 60% reported by Mártin-Sómer et al. [20] for the corresponding configurations. Additional details regarding the ferrioxalate actinometric tests can be found in Fig. SM-3.

The CFD simulations showed that the radiation powers at the reactor's inner wall were 0.97 W, 1.55 W, and 1.60 W for each case, respectively. In the radiation model used in this study, lamp surfaces were treated as opaque to incident radiation, which neglects partial transmission through the quartz envelope and underestimates the radiation reaching the reactor wall, particularly at bench-scale. To account for this limitation, a photon redistribution within the system was considered as a first-order approximation, reflecting the semi-transparent nature of the quartz envelope. Under this adjustment, the predicted incident power increased to 1.26 W (no-reflector), 2.98 W (N = 1), and 3.10 W (N = 3), recovering the experimentally observed trend and improving agreement with actinometric measurements.

As shown by Martín-Sómmer et al. [20], the N = 3 reflector design favors more direct photon trajectories toward the ARZ, whereas in the N = 1 configuration, photons may undergo multiple reflections before reaching the ARZ. Because each reflection involves partial energy losses associated with the reflectivity of the surfaces, the N = 3 geometry allows a larger fraction of the radiation emitted by the lamps to reach the

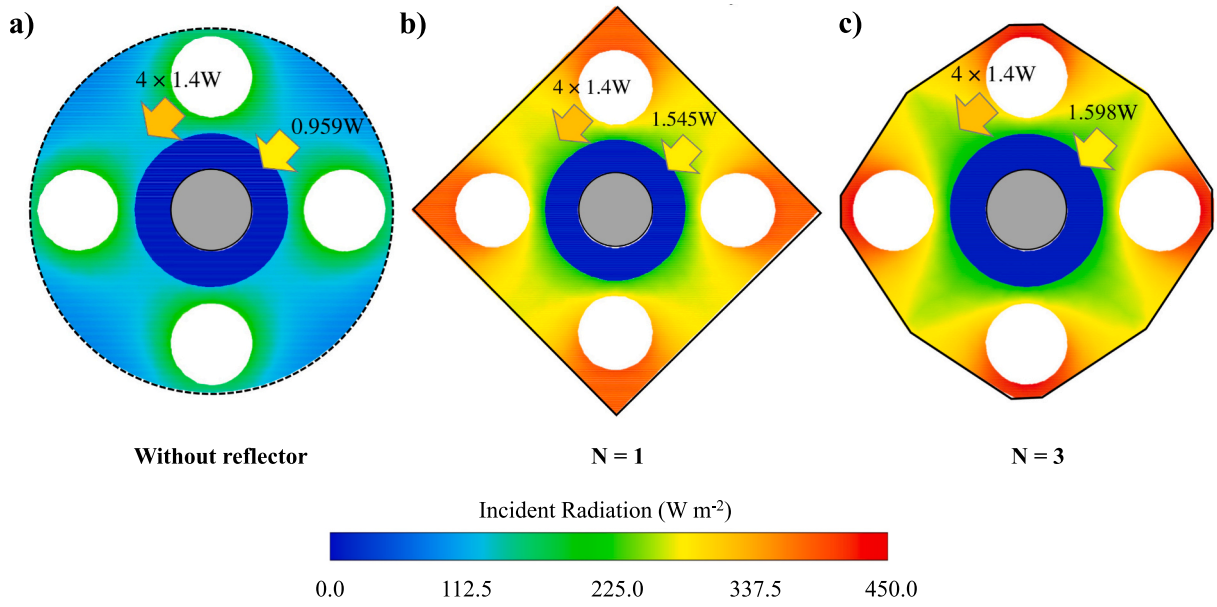

Fig. 4. Spatial distribution of incident radiation flux (W m^{-2}) predicted by the DO model at the reactor mid-section within the ARZ for (a) no-reflector, (b) $N = 1$ geometry, and (c) $N = 3$ reflector configuration.

ARZ with greater intensity. This is observed in the spatial radiation fields (Fig. 4b–c) and in the incident radiation field (Fig. SM-4), where the irradiance is more evenly distributed, and low-irradiance regions are less pronounced than in the N = 1 configuration. Reflector geometry, therefore, affects both the amount of radiation reaching the ARZ and its distribution within the reactor.

3.1.3. *Photodegradation tests*

The efficiency of OMPs oxidation via UVC photolysis was initially evaluated in DW fortified with 10 μg L^{-1} of each target OMP (Table 1), under continuous mode with a τ of 17 s (Table 2). This matrix was selected to isolate the effects of UVC irradiation by minimizing potential interferences from background organic and inorganic constituents. Three reflector configurations were evaluated: (i) no reflector (Exp. #1), (ii) N = 1 reflector (Exp. #2), and (iii) N = 3 reflector (Exp. #3).

As expected, the absence of a reflective surface resulted in the lowest photolytic efficiency. In Exp. #1 (Fig. 5a), only 4 of the 13 target OMPs (Diclofenac, Diuron, Iopromide, and Sulfamethoxazole) present measurable degradation (>10%, considering analytical uncertainty). At a UVC dose of 0.17 kJ L^{-1} (based on actinometric measurements), the 4 target OMPs had an average removal of 62 ± 22%. Incorporating the N = 1 reflector (Exp. #2, Fig. 5a), the UVC dose increased to 0.32 kJ L^{-1}, yielding an average removal of 70 ± 27% for 5 OMPs, with Losartan showing moderate degradation (32 ± 5%) in addition to the 4 OMPs photolyzed already in Exp #1. The N = 3 geometry (Exp. #3, Fig. 5a), corresponding to a UVC dose of 0.36 kJ L^{-1}, provided a slightly higher average degradation for the same OMPs (75 ± 24%). The incorporation of reflective surfaces (Exp. #2 and #3), leading to enhanced photon delivery to the ARZ and an effective UVC dose, showed clear improvements in OMPs degradation performance.

A clear positive correlation was observed between UVC dose and OMPs degradation. Under UVC irradiation, degradation primarily occurs via direct photolysis, in which OMPs absorb photons that excite chromophoric groups, promoting subsequent molecular breakdown. Photolytic degradation is strongly influenced by the photochemical properties of OMPs, particularly the molar absorption coefficient at 254 nm (ε_{254nm}) and the quantum yield at 254 nm (Φ_{254nm}). Compounds with $\varepsilon_{254nm} \geq 10^3$ and/or $\Phi_{254nm} \geq 10^{-1}$ are generally more susceptible to UVC photolysis, whereas those with $\varepsilon_{254nm} \leq 10^2$ and/or $\Phi_{254nm} \leq 10^{-2}$ are more resistant [9].

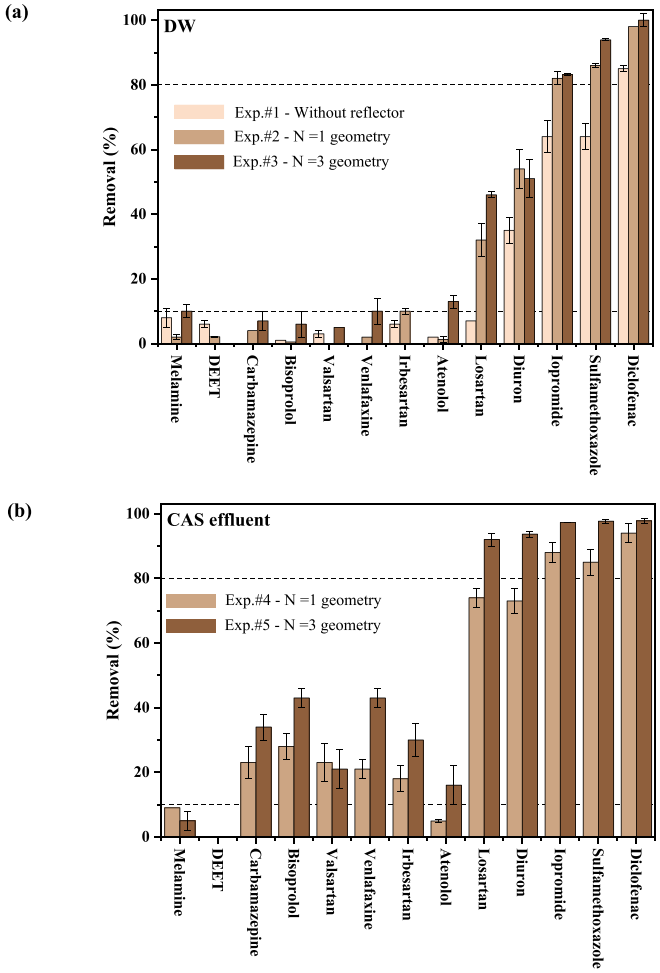

Fig. 5. Removal efficiencies (%) of target OMPs under UVC photolysis in (a) DW and (b) CAS effluent. Additional operating conditions are detailed in Table 2.

The values outlined in Table 1 agree with the outcomes of Exp. #1 – Exp. #3 (Fig. 5a), confirming that Diclofenac, Diuron, Losartan, Sulfamethoxazole, and Iopromide were among the most responsive to UVC, particularly under the N = 3 configuration, which underscores the benefits of enhanced radiation availability. For Losartan and Sulfamethoxazole, in particular, the progressive degradation as the UVC dose increased was clearly observed, reflecting their strong dependence on photon exposure.

Following the DW experiments, photodegradation tests were conducted with a CAS effluent spiked with the same 13 target OMPs (10 μg L^{-1} each), using N = 1 and N = 3 reflectors. Unlike DW experiments, tests without a reflector were not conducted, as CAS effluent contains organic matter and suspended solids that strongly absorb and scatter UVC radiation, limiting the photolysis effectiveness. To enhance the exposure time of contaminants to UVC radiation (3 min 24 s), a partial recirculation strategy was adopted.

This operational approach extended the effective residence time of the treated volume while maintaining constant hydrodynamic conditions in the ARZ, as the total flow rate through the reactor remains unchanged and only the feed-to-recirculation ratio is adjusted. As a result, the treated matrix was exposed to multiple passes through the irradiated zone, increasing the cumulative photon dose without altering the intrinsic flow regime. This effect is particularly relevant for complex matrices such as CAS effluent, where higher irradiation exposure is required to overcome light attenuation and radical scavenging. Similar strategies have also been applied in previous studies [9,18,19].

Given the 12-fold increase in the residence time compared to DW tests, the applied UVC dose was considerably higher, reaching 3.9 kJ L^{-1} for N = 1 geometry and 4.3 kJ L^{-1} for N = 3 geometry. In tests with the CAS effluent, the N = 1 geometry (Exp. #4, Fig. 5b) achieved an average removal of 53 ± 32% across 10 OMPs, while N = 3 improved performance to 60 ± 34% for 11 OMPs (Exp. #5, Fig. 5b). As expected, the more uniform photon distribution provided by N = 3 geometry enhanced the overall OMPs degradation, even under the more challenging optical conditions of real wastewater.

Rodrigues-Silva et al. [18] evaluated the degradation of 14 OMPs (including the 13 investigated here) in CAS effluent fortified with 10 μg L^{-1} of each compound, using an N = 1 reflector made of cardboard covered with standard aluminum foil. Under comparable operating conditions, their actinometric measurements indicated a UVC dose of 3.3 kJ L^{-1}, resulting in an average OMPs removal of approximately 40%. In the present study, the same N = 1 geometry applied MIRO®4 UVC reflective aluminum sheets as the reflective material, yielding a higher actinometric-based UVC dose (3.9 kJ L^{-1}) and a correspondingly improved average removal of 53%. This comparison highlights that, even with identical geometrical configurations, the optical properties of the reflector material directly influence photon availability within the reactor and, consequently, the photolytic performance. Furthermore, the improved results obtained with the N = 3 configuration emphasize the additional benefits of optimizing the reflector geometry, aiming for a more uniform photon distribution and greater photodegradation efficiency, particularly in the treatment of effluents with high light attenuation capacity (such as CAS).

3.2. Pilot-scale tubular membrane photoreactor

3.2.1. RTD analysis

RTD experiments were conducted to evaluate the macromixing associated with the pilot-scale reactor. These experiments provide an independent experimental characterization of the reactor hydrodynamics, complementing CFD analysis. For the tested flow rates (30 and 80 L h^{-1}, $\tau_{theoretical}$ = 1 min 54 s and 42 s, respectively), the experimentally determined average residence times differed by about 10% from the theoretical values. During the RTD experiments, the membrane lumen remained empty and unpressurized, potentially allowing partial liquid diffusion through the membrane pores due to the hydrophilic nature of the material. This effect may contribute to the observed deviation, although its influence remains limited relative to the total reactor volume. The qualitative interpretation of the flow regime is therefore not affected. This limitation is acknowledged and should be addressed in future studies by performing RTD experiments under pressurized membrane conditions.

The experimental RTD curves and their corresponding ADFM fits for flow rates of 30 and 80 L h^{-1} are presented in Fig. 6a and b, respectively. The RTD curves display a single asymmetric peak around $\theta \approx 1$, meaning that the mean residence time is consistent with the nominal hydraulic residence time of the system, followed by tailing toward higher θ values, characteristic of tubular reactors with axial dispersion [34]. The Péclet numbers derived from the ADFM were 24 and 11 for flow rates of 30 L h^{-1} and 80 L h^{-1}, respectively, indicating a non-ideal plug flow with moderate axial dispersion. The decrease in *Pe* with increasing flow rate denotes enhanced longitudinal mixing, consistent with the tangential inlet configuration [26]. This affects tracer dispersion along the annular zone, resulting in D_a values of 0.0032 and 0.0181 m^2 s^{-1} for flow rates of 30 and 80 L h^{-1}, respectively. Accordingly, the flow approaches a mixed regime as the Reynolds number increases.

Values of 0.084 and 0.18 were obtained for the dimensionless variance (σ_θ^2) for flow rates of 30 and 80 L h^{-1}, respectively. According to the axial dispersion model, the dimensionless variance is inversely related to the *Pe* number ($\sigma_\theta^2 = 2/Pe$), suggesting that larger variances indicate

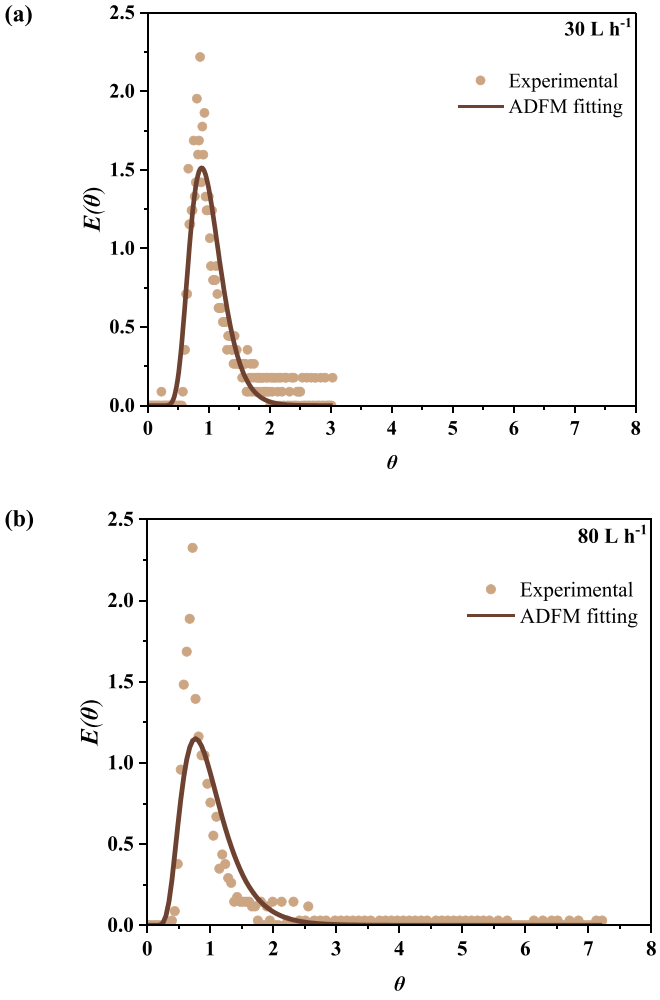

Fig. 6. Experimental vs axial dispersion flow model (ADFM) obtained for the tracer experiments conducted in the tubular membrane photoreactor at pilot-scale at (a) 30 L h^{-1} (Pe = 24; D_a = 0.0032 m^2 s^{-1}) and (b) 80 L h^{-1} (Pe = 11; D_a = 0.0181 m^2 s^{-1}).

stronger axial dispersion. The observed increase in σ_θ^2 at the higher flow rate confirms a greater longitudinal spreading of the tracer within the reactor, which is consistent with the decline in the *Pe* number from 24 to 11. Although the ADFM captures the general shape and dispersion of the RTD curves, deviations remain near the peak and in the tail region. The experimental curves show slightly steeper peaks and longer tails than predicted, indicating non-ideal flow features such as localized recirculation zones or preferential flow paths that are not fully captured by the one-dimensional axial dispersion model.

3.2.2. CFD simulation: flow pattern

Fig. 7 shows the simulated flow pattern within the pilot-scale reactor, including a global perspective of the velocity field and a detailed view of the velocity vectors (Fig. 7a), as well as the pathlines representing fluid trajectories from the reactor inlet (Fig. 7b). The flow pattern closely resembles that of the bench-scale reactor, with strong rotational motion predominantly concentrated near the tangential inlet (at the bottom of the reactor). As the flow progressed upward, the angular velocity decreased due to the frictional dissipation with the wall and the membrane, dampening the flow rotation. Hence, despite the increase in axial length, the fundamental characteristic of the helical flow in the design is preserved.

To further analyze the hydraulics, the spatial evolution of the flow pathlines was examined. These trajectories emphasized helical pattern generated by the tangential inlet (Fig. 8a). Near the inlet, the tightly packed pathlines reflect the strong rotational momentum, which progressively weakens along the reactor length as the rotational energy dissipates. Toward the outlet, an edge effect realigns the streamlines along the axial direction, causing a wider helical spacing that tends to converge, indicating reduced rotational intensity.

The CFD results also enabled the analysis of axial (z-direction) velocity components within the reactor. Regions with zero or negative axial velocities, associated with backmixing or local stagnation, were identified (Fig. 8b, highlighted in red). These zones occurred primarily near the inlet and, to a lesser extent, near the outlet. The volume of these regions increased moderately with the flow rate, occupying approximately 10%–13% of the total reactor volume. This trend is consistent with the reduction in the Péclet number obtained from RTD analysis and the associated increase in axial dispersion at higher flow rates.

3.2.3. CFD simulation: photon field in actinometry

Ferrioxalate actinometry was performed to quantify the incident irradiation under the same reflector configurations previously tested in the bench-scale reactor. The measured incident power values were 10.5 ± 0.5 W, 22.6 ± 0.9 W, and 27.6 ± 0.3 W for the tests conducted with no-reflector, N = 1, and N = 3 geometries, respectively (more details in Fig. SM-5). Hence, among the tested configurations, N = 3 provided the highest optical efficiency, more than doubling the power delivered to the ARZ compared with the no-reflector case. Consequently, this configuration achieved a higher effective power output for the same lamp electrical input, thereby increasing the fraction of emitted radiation delivered to the ARZ. These results are consistent with the trends observed in Section 3.1.2, confirming that the inclusion of reflective surfaces increases photon delivery to the ARZ. Due to the more uniform distribution of photons in the reaction zone and the overall photodegradation performance achieved in the bench-scale reactor, the N = 3 configuration was selected for integration into the pilot-scale reactor.

To complement the experimental data, numerical simulations using

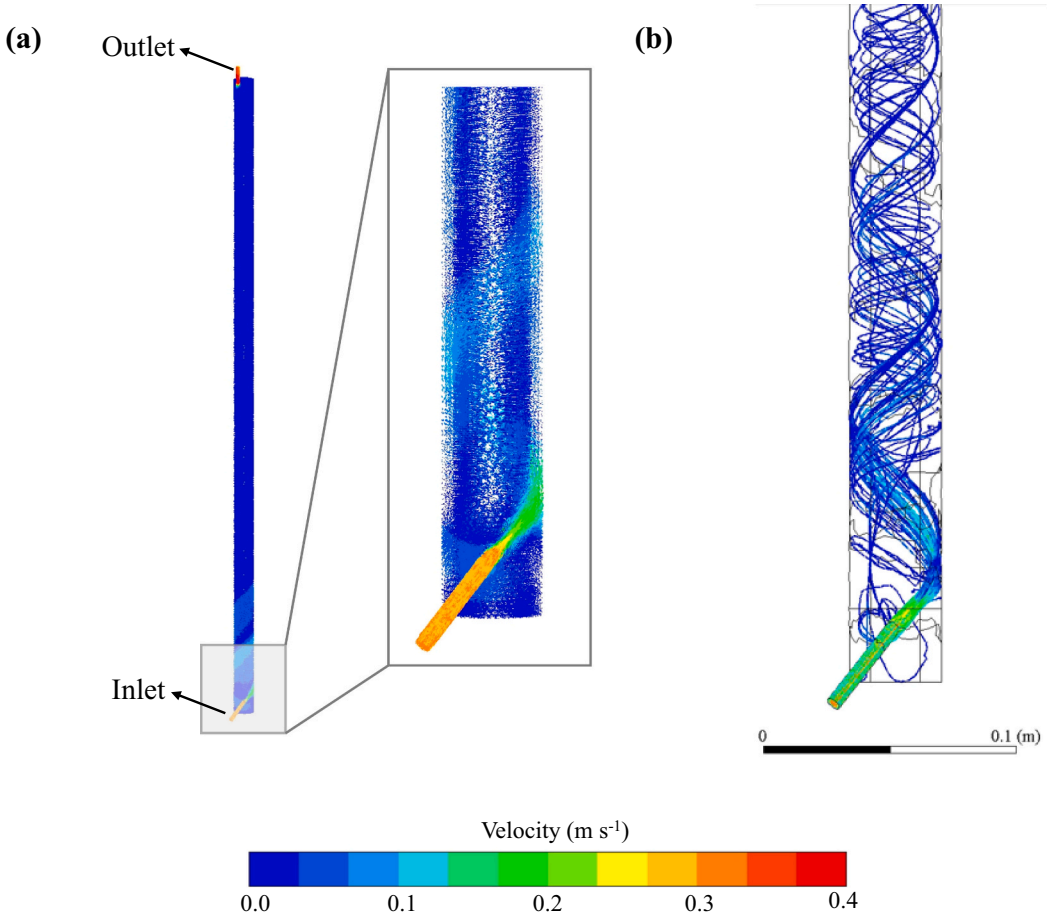

Fig. 7. Distribution of velocity magnitude within the pilot-scale tubular membrane photoreactor at Q_F = 30 L h^{-1} (a) velocity vector map and (b) pathlines trajectories.

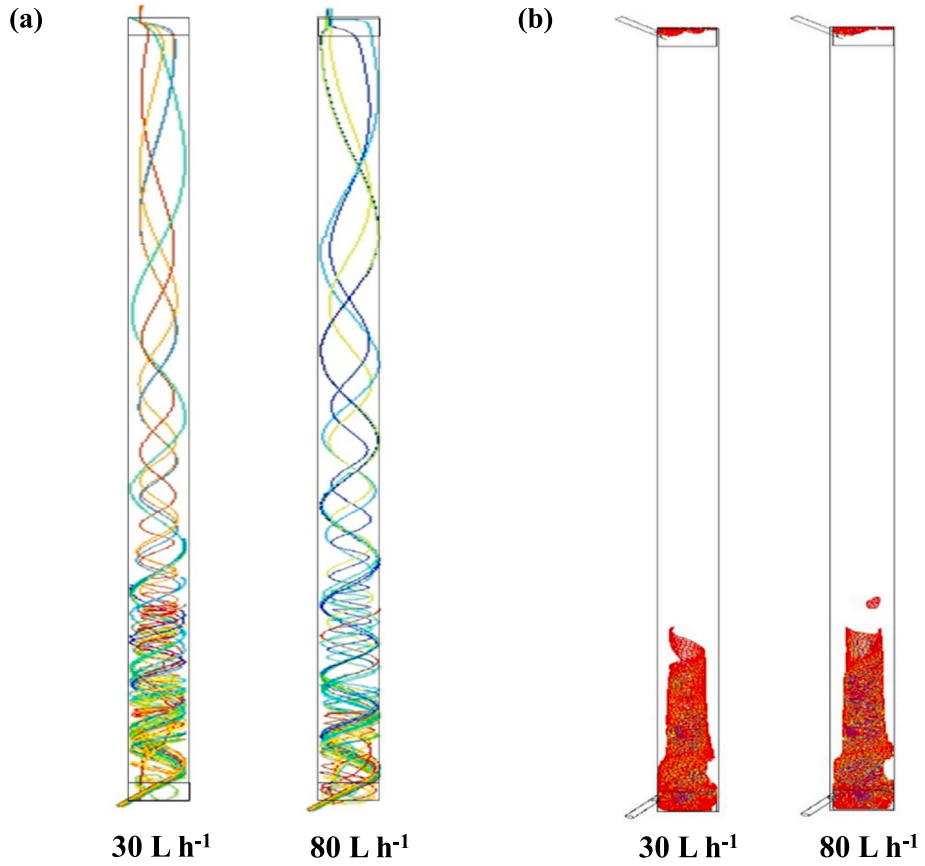

Fig. 8. Flow pattern analysis in the pilot-scale tubular membrane photoreactor at different flow rates, (a) based on the trajectory lines and (b) applying volumes with axial velocities ≤0.

the DO radiation model were used to estimate the distribution and intensity of the photonic field. Fig. 9a displays the external radiation field for the N = 3 configuration, revealing a heterogeneous distribution of photons in the space between the reflector and the reactor wall. As expected, the highest intensities were concentrated in the immediate vicinity of the lamps, while lower values were detected near the reactor wall. This gradient is clarified in the radiation field through a cross-section halfway along the axial axis of the device. Comparison with

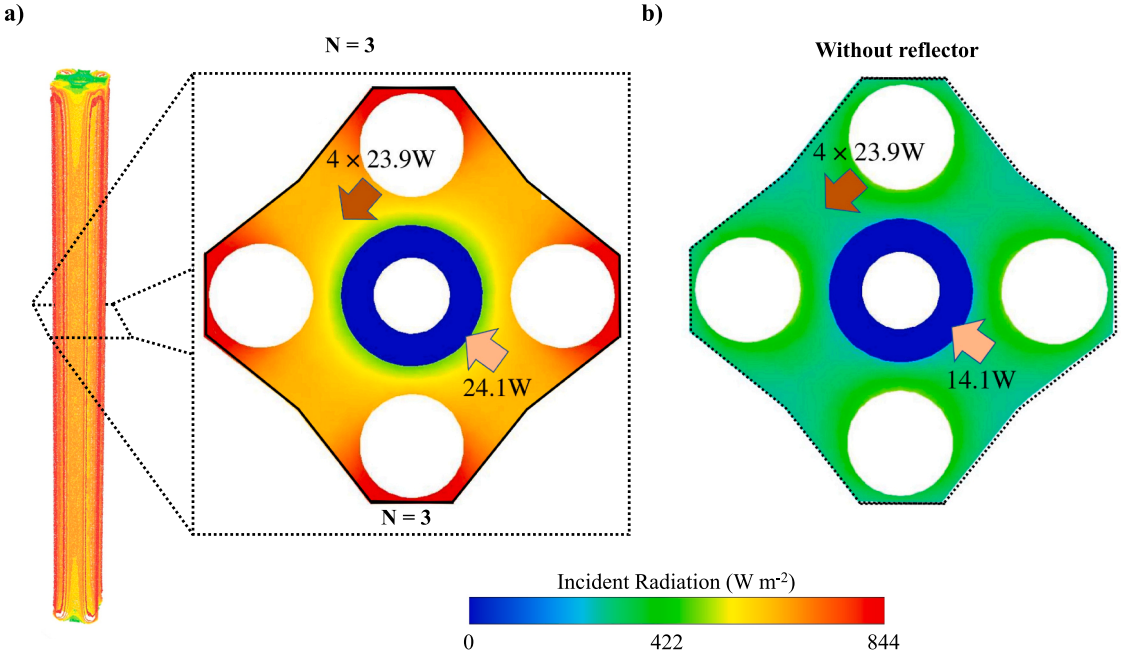

Fig. 9. Incident radiation field in the pilot-scale tubular membrane photoreactor obtained by CFD at (a) N = 3 geometry from a global perspective and at a cross-section at the midpoint of the reactor, and (b) no-reflector.

the no-reflector configuration (Fig. 9b) demonstrates that the N = 3 reflector increased the radiation reaching the quartz wall (14.1 W vs 24.1 W), confirming improved photon redirection toward the ARZ.

The combined analysis of actinometric data and CFD-based radiative transfer modeling confirmed, once again, that the photonic field distribution was strongly influenced by the presence and configuration of reflectors. Furthermore, the closer alignment between simulated and experimental results at the pilot-scale suggests that the simplified modeling assumptions adopted - such as ideal reflective behavior and simplified lamp emission profiles assuming uniform intensity along the lamp length but radial emission into the reactor domain - are better suited to larger-scale geometries, where the relative impact of boundary uncertainties is reduced.

3.2.4. Photodegradation of venlafaxine

3.2.4.1. UVC photolysis. Applying the N = 3 reflector, UVC photolysis experiments (Exp. #6 to #8, Fig. 10) in DW fortified with VLX (20 mg L^{-1}) confirmed that UVC radiation alone was insufficient for an effective VLX degradation. At a flow rate of 30 L h^{-1} (Exp. #6, UVC dose of 3.1 kJ L^{-1}), approximately 20 ± 1% removal was achieved, while at 45 L h^{-1} (Exp. #7, UVC dose of 2.1 kJ L^{-1}) and 80 L h^{-1} (Exp. #8, UVC dose of 1.2 kJ L^{-1}), VLX degradation decreased to 11.3 ± 0.5% and 7 ± 1%, respectively. This trend underscores the importance of residence time in enhancing contaminant exposure to photons: lower flow rates extend the contact time between pollutants and radiation, thereby improving degradation efficiency under direct photolysis conditions. The limited photolysis observed for VLX is expected, given its low sensitivity to UVC radiation, as indicated by its low ε_{254nm} and Φ_{254nm} values (Table 1).

Following, CFD simulations were performed to analyze the spatial VLX concentration profiles under the operating conditions of Exp. #6 (30 L h^{-1}). Figs. 11a and SM-6 display the axial concentration profiles normalized to the inlet concentration of VLX ($[VLX]/([VLX]_0)$ at two radial positions: membrane surface ($[VLX]_{MS}$) and quartz wall ($[VLX]_{QW}$), represented in dotted and solid red lines, respectively. The small gap between these two curves reflects a minor radial concentration gradient, confirming effective radial mixing induced by the helical flow pattern. The cross-sectional average ($[VLX]_{CS}$, dashed red line) lies between both profiles but is closer to the quartz wall. Only a modest decline in VLX concentration was observed along the reactor length, attributable solely to direct photolysis. According to the kinetic laws

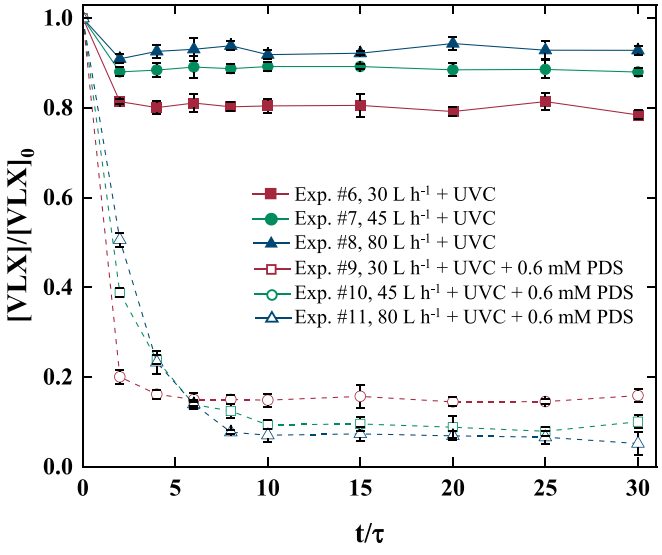

Fig. 10. VLX concentration profiles under different flow rates and treatment conditions in the pilot-scale tubular membrane photoreactor with $N = 3$ geometry. Additional operating conditions are detailed in Table 2.

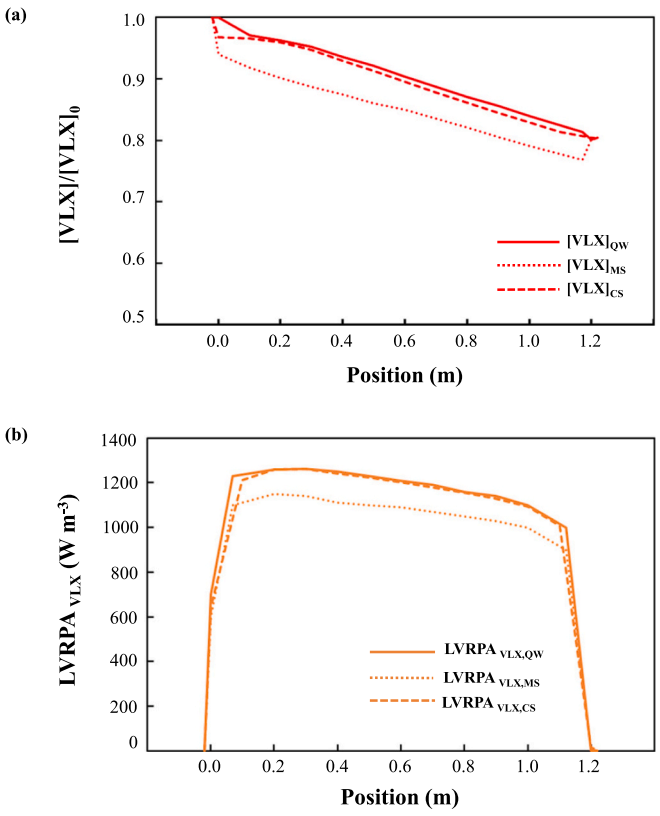

Fig. 11. CFD simulation results at photolysis-only conditions (Exp. #6: Q_F = 30 L h^{-1}; N = 3 reflector): (a) normalized VLX concentration and (b) LVRPA of VLX profile along the reactor axis. Legend: CS – cross-section; MS – membrane surface; QW – quartz wall.

(Eq. (8), of Section 2.3.3), VLX photolysis dependents on the LVRPA within the ARZ. In this sense, Figs. 11b and SM-6 show the LVRPA profiles for VLX at the same radial positions: membrane surface ($LVRPA_{VLX,MS}$), quartz wall ($LVRPA_{VLX,QW}$), and cross-section average ($LVRPA_{VLX,CS}$), represented in dotted, solid, and dashed orange lines, respectively. As discussed in Section 3.2.3, the lower photon flux reaching the membrane surface limits the local photolysis rate, while maximum LVRPA values are observed in the reactor midsection that gradually drop along the reactor length as photon absorption progresses during photolysis.

3.2.4.2. UVC/PDS – membrane dosing. To assess the consistency and verify the integrity of oxidant dosing through the membrane system, preliminary non-reactive tests were performed without UVC irradiation and using DW as the feed solution. PDS was introduced at concentrations of 1, 2, and 3 mM, and the corresponding outlet concentrations were monitored over time (Fig. SM-7). The PDS concentration gradually increased over time, reaching steady-state at approximately $t/\tau = 7.8$, after which the outlet PDS concentrations closely aligned with the theoretical values (represented by the dotted lines). These results support that the membrane maintained consistent and effective permeation properties across all oxidant dosages tested. PDS permeation tests were periodically repeated throughout the study to ensure steady membrane performance over time.

Under UVC radiation, the addition of PDS substantially improved VLX removal, with degradations of 90 ± 2%, 85 ± 1%, and 93 ± 1% observed at flow rates of 30, 45, and 80 L h^{-1}, respectively (Exp. #9, Exp. #10 and Exp. #11, Fig. 10). In the presence of PDS, VLX degradation is primarily driven by sulfate radicals ($SO_4^{\bullet-}$), generated through PDS activation by UVC radiation (Eq. (12)). Unlike direct photolysis, this radical-mediated process occurs at an extremely fast reaction rate

($k_{SO_4^{\bullet-},VLX} = 3.5 \times 10^9\ M^{-1}\ s^{-1}$ [9]). As a result, the process becomes less sensitive to residence time, explaining the similar degradation efficiencies observed across flow rates. These results are driven by the UVC/PDS process, with the photoreactor ensuring the hydrodynamic and photonic conditions required for oxidant activation.

$$S_2O_8^{2-} + h\upsilon \rightarrow 2SO_4^{\bullet-} \quad (12)$$

In this system, PDS is delivered uniformly into the reaction zone through the membrane, while VLX enters with the feed stream. Both species absorb UVC radiation and are coupled through competition for photon absorption. VLX absorption leads to direct photolysis, resulting in only modest degradation (approximately 20% under UVC alone, as indicated in Section 3.2.4.1). In contrast, PDS absorption promotes its photochemical activation and the generation of $SO_4^{\bullet-}$ radicals, the primary oxidizing agents responsible for VLX oxidation. Photon absorption by VLX reduces the fraction of photons available for PDS activation, thereby limiting radical production and indirectly affecting VLX degradation. Thus, VLX and PDS serve different roles in photochemistry, their interaction through competition for light photons connects their effects on the overall degradation process.

CFD simulations under the conditions of Exp. #9 confirmed a near-uniform introduction of PDS along the ceramic membrane surface, leading to high concentrations near the membrane and diffusion toward the bulk flow following a helical trajectory, resulting in a pronounced radial concentration gradient (Fig. 12a). Photon availability also varied across the reactor cross-section, with higher photon concentration near the quartz wall (the external surface of the reaction system) due to its proximity to the UVC source (Fig. 12b). Consequently, PDS activation is spatially non-uniform, reinforcing the radial gradients in both oxidant concentration and reaction rates. A similar phenomenon occurs with VLX, although the gradient is smoother, since its inlet distribution results in a more homogeneous distribution across the cross-section (Fig. 12a, red lines). However, near the reactor inlet, PDS concentration is initially low due to its absence from the feed stream. As a result, in this small inlet section, radial diffusion governs the transport of PDS into the main flow, where the helical velocity field began to develop (border effect). A similar effect may appear at the outlet, where flow patterns disturbances reduced mixing uniformity. Despite these localized gradients, VLX degradation reached approximately 90% in Exp. #9, as evidenced by the concentration profiles in Fig. 12a. A summary of the 3D fields for incident radiation, VLX concentration, and $LVRPA_{VLX}$ within the pilot-scale tubular membrane photoreactor during the photodegradation of VLX with UVC/PDS is shown in Fig. SM-8.

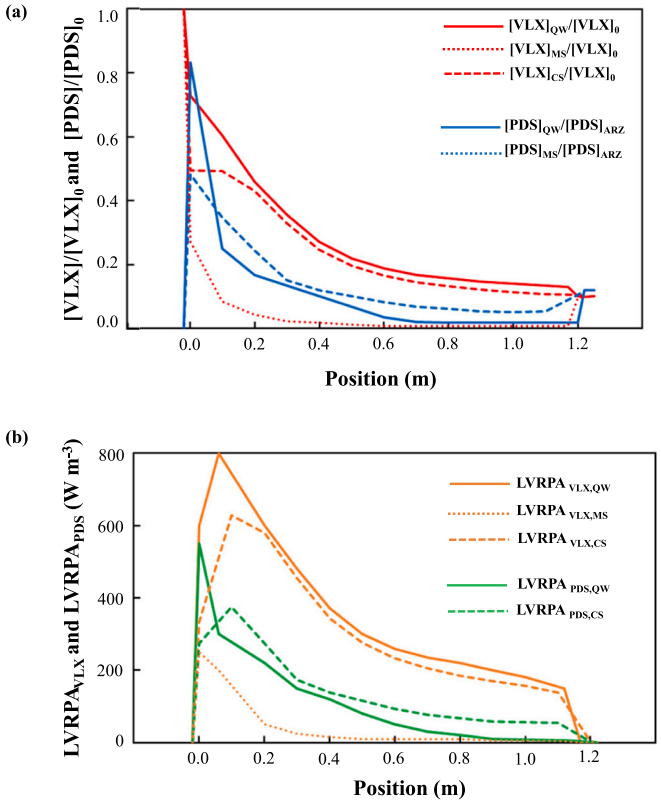

Fig. 12. CFD simulation results at UVC/PDS conditions (Exp. #9: Q_F = 30 L h^{-1}; N = 3 reflector): (a) normalized VLX and PDS concentrations, and (b) LVRPA of VLX and PDS. Legend: CS – cross-section; MS – membrane surface; QW – quartz wall.

Although no VLX oxidation experiments were carried out without a reflector, simulations were conducted to evaluate its impact on the reaction performance. The model predicts a VLX conversion of 85% in the absence of a reflector, compared to 93% with the N = 3 geometry (Exp. #9). At first glance, this minor difference might suggest a small effect of the reflector on the process effectiveness. However, a detailed analysis revealed that this similarity in the conversion values stemmed from a compensatory effect. According to the simulation results, without a reflector, the total incident radiation was only 14.1 W, which corresponds to approximately 60% of that achieved with the N = 3 geometry (Fig. 9a and b). Nevertheless, this lower photon input proved sufficient for $SO_4^{\bullet-}$ radicals generation to sustain high VLX oxidation levels. Notwithstanding, the use of reflectors remains advantageous as this approach maximizes the use of available radiation, thereby improving photon utilization efficiency and effective PDS activation with lower residual concentrations, thus enhancing process sustainability, an important advantage for real-scale applications.

4. Conclusions

This work combined CFD and experimental data to examine the hydrodynamic and photonic behavior of a tubular membrane photoreactor operated under UVC irradiation at bench- and pilot-scale. The results showed that reactor performance was governed by the interaction between reflector geometry, helical flow, and membrane-based oxidant dosing. Initial bench-scale testing demonstrated that the reflector was not a marginal design element, as the N = 3 configuration increased photon delivery to the annular reaction zone and produced a more even radiation field, resulting in the highest photolytic removal of the selected OMPs. This effect became more evident in CAS effluent, where light attenuation imposed more demanding conditions. At pilot-scale, RTD analysis and CFD showed that the elongated reactor retained the main hydrodynamic features of the bench-scale configuration, namely helical flow, moderate axial dispersion, and localized backmixing near the inlet and outlet. Under UVC alone, VLX removal remained limited and residence-time dependent. Once PDS was introduced through the membrane, removal increased markedly and remained high across the tested flow range, indicating that the reactor configuration provided suitable conditions for oxidant activation under continuous operation. Under the tested conditions, the pilot-scale unit operated within a treatment capacity of 0.7–1.9 $m^3\ day^{-1}$ while maintaining high VLX removal (≥85%) in the UVC/PDS system. Since the pilot-scale reaction study was conducted with VLX in synthetic water, further work should examine the system performance in more complex wastewater matrices. Direct experimental validation of the internal spatial radiation field would also strengthen the interpretation of the photon distribution predicted by the CFD model.

CRediT authorship contribution statement

Carla S. Santos: Writing – original draft, Validation, Methodology, Investigation, Formal analysis, Data curation, Conceptualization. **Paulo H. Marrocos:** Writing – review & editing, Validation, Formal analysis. **Claudio Passalía:** Writing – review & editing, Validation, Software,

Investigation, Formal analysis. **Marisol D. Labas:** Writing – review & editing, Validation, Software, Formal analysis. **Rodolfo J. Brandi:** Writing – review & editing, Validation, Software, Methodology, Formal analysis. **Rosa Montes:** Writing – review & editing, Methodology, Investigation, Formal analysis, Data curation. **Rosario Rodil:** Writing – review & editing, Validation, Resources, Methodology. **José B. Quintana:** Writing – review & editing, Validation, Resources. **Ana I. Gomes:** Writing – review & editing, Visualization, Validation, Supervision, Formal analysis, Conceptualization. **Vítor J.P. Vilar:** Writing – review & editing, Visualization, Supervision, Resources, Funding acquisition, Conceptualization.

Declaration of competing interest

The authors declare the following financial interests/personal relationships which may be considered as potential competing interests: Given Vítor J. P. Vilar role as Coordinating Editor, had no involvement in the peer review of this article and had no access to information regarding its peer review. Full responsibility for the editorial process for this article was delegated to another journal editor. If there are other authors, they declare that they have no known competing financial interests or personal relationships that could have appeared to influence the work reported in this paper.

Acknowledgments

This work was supported by (i) EU and Bundesministerium für Bildung und Forschung, Germany, Ministero dell'Università e della Ricerca, Italy, Agencia Estatal de Investigación, Spain, Fundação para a Ciência e a Tecnologia (FCT), Portugal, Norges forskningsråd, Norway, Water Research Commission, South Africa for funding, in the frame of the collaborative international consortium SERPIC, financed under the ERA-NET AquaticPollutants Joint Transnational Call (GA N° 869178; Reference Aquatic/0002/2020 with DOI 10.54499/Aquatic/0002/2020), an integral part of the activities developed by the Water, Oceans and AMR Joint Programming Initiatives, (ii) Spanish Agencia Estatal de Investigación – MCIN/AEI/10.13039/501100011033 (ref. PID2024-156804OB-C32), (iii) regional funds Xunta de Galicia (ED431C 2025/21) and (iv) Universidad Nacional del Litoral (UNL, Project CAI+D-2024 85520240100029LI). This research was also supported by Fundação para a Ciência e a Tecnologia, I.P./MECI through national funds: LSRE-LCM, UID/50020/2025 (https://doi.org/10.54499/UID/50020/2025); and ALiCE, LA/P/0045/2020 (https://doi.org/10.54499/LA/P/0045/2020). Carla S. Santos and Paulo H. Marrocos acknowledge the PhD scholarship funded by FCT (2022.10796.BD, DOI: 10.54499/2022.10796.BD and 2022.10437.BD, DOI: 10.54499/2022.10437.BD).

Appendix A. Supplementary data

Supplementary data to this article can be found online at https://doi.org/10.1016/j.cej.2026.176188.

Data availability

Data will be made available on request.

References

[1] E.D. 2024/3019, Directive (EU) 2024/3019 of the European Parliament and of the Council of 27 November 2024 Concerning Urban Wastewater Treatment, 2024.
[2] J. Ianes, S. Piraldi, B. Cantoni, M. Antonelli, Micropollutants removal, residual risk, and costs for quaternary treatments in the framework of the Urban Wastewater Treatment Directive, Water Res. X 29 (2025), https://doi.org/10.1016/j.wroa.2025.100334.
[3] M. Włodarczyk-Makuła, B. Tchórzewska-Cieślak, J.R. Rak, Risk assessment method for pharmaceutics removal in treated wastewater – challenges of new Directive (EU) on urban wastewater treatment, Sci. Total Environ. 996 (2025), https://doi.org/10.1016/j.scitotenv.2025.180141.
[4] N. Abd Rahman, C.E. Choong, S. Pichiah, I.W. Nah, J.R. Kim, S.-E. Oh, Y. Yoon, E. H. Choi, M. Jang, Recent advances in the TiO_2 based photoreactors for removing contaminants of emerging concern in water, Sep. Purif. Technol. 304 (2023), https://doi.org/10.1016/j.seppur.2022.122294.
[5] D. Ghime, P. Ghosh, Advanced oxidation processes: a powerful treatment option for the removal of recalcitrant organic compounds, in: Advanced Oxidation Processes - Applications, Trends, and Prospects, 2020, https://doi.org/10.5772/intechopen.90192.
[6] S. Guerra-Rodríguez, E. Rodríguez, J. Rodríguez-Chueca, Pilot-scale regeneration of wastewater through intensified sulfate radical-based advanced oxidation processes (PMS/UV-A, PMS/H_2O_2/UV-A, and PMS/O_3): Inactivation of bacteria and mechanistic considerations, Chem. Eng. J. 469 (2023), https://doi.org/10.1016/j.cej.2023.143859.
[7] F. Mortezazadeh, M. Ahmadi Nasab, A. Javid, F. Changani, M.H. Dehghani, A review of UV-based advanced oxidation processes in wastewater treatment systems, Desalin. Water Treat. 323 (2025), https://doi.org/10.1016/j.dwt.2025.101388.
[8] L. Rizzo, T. Agovino, S. Nahim-Granados, M. Castro-Alférez, P. Fernández-Ibáñez, M.I. Polo-López, Tertiary treatment of urban wastewater by solar and UV-C driven advanced oxidation with peracetic acid: Effect on contaminants of emerging concern and antibiotic resistance, Water Res. 149 (2019) 272–281, https://doi.org/10.1016/j.watres.2018.11.031.
[9] A.R. de Olivera, C.S. Santos, I.F. Mena, M.A. Montiel, R. Montes, J.B. Quintana, R. Rodil, A.I. Gomes, F.C. Moreira, J. Gäbler, L. Schäfer, C. Sáez, M.A. Rodrigo, V.J. P. Vilar, Integration of a 3D-printed electrochemical reactor with a tubular membrane photoreactor to promote sulfate-based advanced oxidation processes, Chem. Eng. J. 500 (2024), https://doi.org/10.1016/j.cej.2024.156900.
[10] S. Guerra-Rodríguez, E. Rodríguez, D. Singh, J. Rodríguez-Chueca, Assessment of sulfate radical-based advanced oxidation processes for water and wastewater treatment: a review, Water 10 (2018), https://doi.org/10.3390/w10121828.
[11] K. Tian, L. Hu, L. Li, Q. Zheng, Y. Xin, G. Zhang, Recent advances in persulfate-based advanced oxidation processes for organic wastewater treatment, Chin. Chem. Lett. 33 (2022) 4461–4477, https://doi.org/10.1016/j.cclet.2021.12.042.
[12] J.C. Espíndola, R.O. Cristóvão, S.R.F. Araújo, T. Neuparth, M.M. Santos, R. Montes, J.B. Quintana, R. Rodil, R.A.R. Boaventura, V.J.P. Vilar, An innovative photoreactor, FluHelik, to promote UVC/H_2O_2 photochemical reactions: tertiary treatment of an urban wastewater, Sci. Total Environ. 667 (2019) 197–207, https://doi.org/10.1016/j.scitotenv.2019.02.335.
[13] J. Mei, X. Gao, J. Zou, F. Pang, Research on photocatalytic wastewater treatment reactors: design, optimization, and evaluation criteria, Catalysts 13 (2023), https://doi.org/10.3390/catal13060974.
[14] F. Gaulhofer, H. Becker, A. Peschl, D. Ziegenbalg, Modelling the impact of mass transport in a miniplant photoreactor, React. Chem. Eng. 9 (2024) 3231–3247, https://doi.org/10.1039/d4re00192c.
[15] Z. Khan, M. Kamal, J. Jaafar, F. Mir, G.U. Rehman, A.A. Khan, A.F. Ismail, T. Matsuura, M.H.D. Othman, M.A. Rahman, Recent advances in photoreactor designs for the degradation of persistent organic contaminants with influential effects of configuration and parameters: a review, J. Water Process Eng. 69 (2025), https://doi.org/10.1016/j.jwpe.2024.106825.
[16] V.J.P. Vilar, P. Alfonso-Muniozguren, J.P. Monteiro, J. Lee, S.M. Miranda, R.A. R. Boaventura, Tube-in-tube membrane microreactor for photochemical UVC/H_2O_2 processes: A proof of concept, Chem. Eng. J. 379 (2020), https://doi.org/10.1016/j.cej.2019.122341.
[17] R.M. Castellanos, J. Paulo Bassin, M. Dezotti, R.A.R. Boaventura, V.J.P. Vilar, Tube-in-tube membrane reactor for heterogeneous TiO_2 photocatalysis with radial addition of H_2O_2, Chem. Eng. J. 395 (2020), https://doi.org/10.1016/j.cej.2020.124998.
[18] F. Rodrigues-Silva, C.S. Santos, J.A. Marrero, R. Montes, J.B. Quintana, R. Rodil, O. C. Nunes, M.C.V.M. Starling, C.C. Amorim, A.I. Gomes, V.J.P. Vilar, Continuous UV-C/H_2O_2 and UV-C/Chlorine applied to municipal secondary effluent and nanofiltration retentate: Removal of contaminants of emerging concern, ecotoxicity, and reuse potential, Chemosphere 361 (2024), https://doi.org/10.1016/j.chemosphere.2024.142355.
[19] C. Santos, M. Herraiz-Carboné, E. Lacasa, C. Sáez, R. Montes, J. Benito Quintana, R. Rodil, A.I. Gomes, V.J.P. Vilar, Continuous-flow titration of low iron doses to promote photo-Fenton and photo-Fenton-like processes at neutral pH, Chem. Eng. J. 476 (2023), https://doi.org/10.1016/j.cej.2023.146655.
[20] M. Martín-Sómer, J. Moreira, C. Santos, A.I. Gomes, J. Moreno-SanSegundo, V.J. P. Vilar, J. Marugán, Reflector design for the optimization of photoactivated processes in tubular reactors for water treatment, J. Environ. Chem. Eng. 11 (2023), https://doi.org/10.1016/j.jece.2023.110609.
[21] J. Chai, H. Su, X. Li, Y. Zhang, D. Xiao, J. Kang, A. Dong, Computational fluid dynamics (CFD) modeling and application for cleaning of food-contact surfaces: A review, J. Food Process Eng. 47 (2024), https://doi.org/10.1111/jfpe.14605.
[22] N. Hanspal, S.A. Cryer, The use of computational fluid dynamics (CFD) within the agricultural industry to address general and manufacturing problems, Fluids 9 (2024), https://doi.org/10.3390/fluids9080186.
[23] H.H. Hu, Computational fluid dynamics, in: Fluid Mechanics, 2012, pp. 421–472, https://doi.org/10.1016/b978-0-12-382100-3.10010-1.
[24] R. Peralta Muniz Moreira, G. Li Puma, Multiphysics computational fluid-dynamics (CFD) modeling of annular photocatalytic reactors by the discrete ordinates method (DOM) and the six-flux model (SFM) and evaluation of the contaminant intrinsic kinetics constants, Catal. Today 361 (2021) 77–84, https://doi.org/10.1016/j.cattod.2020.01.012.
[25] A. Qudoos, T.L. Chew, M. Abro, P.C. Oh, L.D. Anbealagan, M.A. Bustam, C.D. Ho, Z.A. Jawad, Q.H. Ng, Review on computational fluid dynamics (CFD) modeling and

simulation of CO_2 adsorption, Results Eng. 28 (2025), https://doi.org/10.1016/j.rineng.2025.107336.
[26] M.P. Caixeta, P.H. Marrocos, I.S. Fernandes, V.J.P. Vilar, R.J. Santos, Hydrodynamic investigation of a tube-in-tube membrane reactor/contactor module using CFD simulation, Chem. Eng. J. 519 (2025), https://doi.org/10.1016/j.cej.2025.165376.
[27] D. Borrás-Jiménez, W. Silva-López, C. Nieto-Londoño, Towards the configuration of a photoelectrocatalytic reactor: part 2—selecting photoreactor flow configuration and operating variables by a numerical approach, Nanomaterials 12 (2022), https://doi.org/10.3390/nano12173030.
[28] C. Luo, J. Ma, J. Jiang, Y. Liu, Y. Song, Y. Yang, Y. Guan, D. Wu, Simulation and comparative study on the oxidation kinetics of atrazine by UV/H_2O_2, UV/HSO_5^- and UV/$S_2O_8^{2-}$, Water Res. 80 (2015) 99–108, https://doi.org/10.1016/j.watres.2015.05.019.
[29] R. Montes, S. Méndez, N. Carro, J. Cobas, N. Alves, T. Neuparth, M.M. Santos, J. B. Quintana, R. Rodil, Screening of contaminants of emerging concern in surface water and wastewater effluents, assisted by the persistency-mobility-toxicity criteria, Molecules 27 (2022), https://doi.org/10.3390/molecules27123915.
[30] P. Verlicchi, V. Grillini, E. Lacasa, E. Archer, P. Krzeminski, A.I. Gomes, V.J. P. Vilar, M.A. Rodrigo, J. Gäbler, L. Schäfer, Selection of indicator contaminants of emerging concern when reusing reclaimed water for irrigation — A proposed methodology, Sci. Total Environ. 873 (2023), https://doi.org/10.1016/j.scitotenv.2023.162359.
[31] M.M. Pituco, P.H. Marrocos, S. Méndez, R. Montes, R. Rodil, F.C. Moreira, V.J. P. Vilar, Ozone injection system based on NETmix technology for quaternary treatment of urban wastewater, J. Environ. Chem. Eng. 13 (2025), https://doi.org/10.1016/j.jece.2025.115465.
[32] M.A. Prada-Vásquez, M.M. Pituco, M.P. Caixeta, S.A. Cardona Gallo, A.M. Botero-Coy, F. Hernández, R.A. Torres-Palma, V.J.P. Vilar, Ozonation using a stainless-steel membrane contactor: Gas-liquid mass transfer and pharmaceuticals removal from secondary-treated municipal wastewater, Chemosphere 349 (2024), https://doi.org/10.1016/j.chemosphere.2023.140888.
[33] E.C. Lumbaque, D.S. Lüdtke, D.D. Dionysiou, V.J.P. Vilar, C. Sirtori, Tube-in-tube membrane photoreactor as a new technology to boost sulfate radical advanced oxidation processes, Water Res. 191 (2021), https://doi.org/10.1016/j.watres.2021.116815.
[34] O. Levenspiel, Chemical reaction engineering, Ind. Eng. Chem. Res. 38 (1999) 4140–4143, https://doi.org/10.1021/ie990488g.
[35] L. Schaare, A. Rave, R. Kuwertz, G. Fieg, M. Skiborowski, Axial dispersion modelling of the residence time distribution in a millistructured plate reactor, Chem. Eng. Process. Process Intensif. 213 (2025), https://doi.org/10.1016/j.cep.2025.110295.
[36] N.E.B. Briggs, J. McGinty, C. McCabe, V. Raval, J. Sefcik, A.J. Florence, Heat transfer and residence time distribution in plug flow continuous oscillatory baffled crystallizers, ACS Omega 6 (2021) 18352–18363, https://doi.org/10.1021/acsomega.1c02215.
[37] A. Inc, ANSYS Fluent Theory Guide, Release 2023 R1 (Canonsburg, PA, USA), 2023.
[38] M.T. Nechita, G.D. Suditu, A.C. Puițel, E.N. Drăgoi, Residence time distribution: literature survey, functions, mathematical modeling, and case study—diagnosis for a photochemical reactor, Processes 11 (2023), https://doi.org/10.3390/pr11123420.
[39] P. Sperle, A. Mirlach, K. Linden, U. Hübner, J.E. Drewes, An actinometric method to characterize performance of reflecting UVC reactors used for water treatment, Water Res. 230 (2023), https://doi.org/10.1016/j.watres.2022.119543.